ACCEPTED

Shen Long, Timothy C. W. Lau, Alfonso Chinnici, Zhao Feng Tian, Bassam B. Dally and Graham J. Nathan
Characteristics of swirling and precessing flows generated by multiple confined jets

http://hdl.handle.net/2440/121480

Characteristics of swirling and precessing flows generated by multiple confined jets

Shen Long,[a)] Timothy C.W. Lau, Alfonso Chinnici, Zhao Feng Tian, Bassam B. Dally, and Graham J. Nathan

Centre for Energy Technology, School of Mechanical Engineering, the University of Adelaide, Adelaide,

South Australia 5005, Australia

An experimental study is reported of the interaction between multiple iso-thermal jets within a cylindrical chamber under conditions relevant to a wide range of engineering applications, including the confined swirl combustors, industrial mixers and concentrated solar thermal devices. The Particle Image Velocimetry (PIV) technique was used to investigate the swirling and precessing flows generated with four rotationally-symmetric inlet pipes at a fixed nozzle Reynolds number of $Re_D = 10,500$ for two configurations of swirl angle ($5°$ and $15°$) and two alternative tilt angles ($25°$ and $45°$). The measurements reveal three distinctive rotational flow patterns within the external recirculation zone (ERZ) and the central recirculation zone (CRZ) for these configurations. It was found that the mean and root-mean-square flow characteristics of the swirl within the chamber depend strongly on the relative significance of the ERZ and CRZ, with the swirling velocity being higher in the CRZ than that in the ERZ. A precessing vortex core (PVC) was identified for all experimental conditions considered here, although its significance was less for the cases with a dominant CRZ.

I. INTRODUCTION

Devices that utilize multiple-jets within a confined environment are commonly used in a wide range of scientific and industrial applications, such as gas turbine engines[1], solar cavity receivers[2], separated-jet combustors[3] and ventilation systems[4]. Furthermore, the details of the flow-field within them can have a significant influence on their system performance and thermal efficiency. However, despite their importance, the internal flow within these systems has not been well characterized due to their greater complexity relative to a single round free jet[5]. Recently, a series of investigations has provided new details of these flows[6-8], such as their large-scale flow regimes and recirculation rates. Nevertheless, some important characteristics of the swirling flow configurations, notably of the presence of any precessing vortex core (PVC)[9] within them, are still not fully understood. Hence, the present investigation aims to address key gaps in understanding of these classes of flow through detailed measurements of the flow velocity within a Multiple Impinging Jet in a Cylindrical Chamber (MIJCC), which has geometrical relevance to the Hybrid Solar Receiver Combustor (HSRC) under development at the University of Adelaide[6-8, 10-12].

While a range of configurations of the MIJCC are available, one of the most common is that which employs rotationally-symmetric nozzles configured in an annular ring aligned with an inclination angle (α_j) relative to the axis of the cavity and/or at an azimuthal angle (θ_j) to the axis of the burner. This configuration generates a swirling flow within the main cavity. Previous studies of the flow-field within the MIJCC found that the two angles that characterize the jet's orientation (α_j and θ_j) and the chamber aspect ratio (L_c/D_c, where L_c refers to the chamber length and D_c is the chamber diameter) have a controlling influence on the mean and turbulent flow-fields[6, 7]. However, while these studies provide useful information, they are limited to the velocity data within the axial

---

a)   Author to whom correspondence should be addressed. Electronic mail: shen.long@adelaide.edu.au

plane of the main chamber (across the chamber axis). That is, no quantitative data are available of the tangential velocity (U_θ) within the radial planes (orthogonal to the chamber axis), despite the swirling component typically having the largest magnitude in high-swirl flows[13-15]. Additionally, no comprehensive data set of velocity measurements suitable for the development of computational models is presently available for the MIJCC and relevant configurations[16]. Hence, the overall aim of the present study is to provide new quantitative understanding of the flow regimes within a cylindrical chamber with multiple interacting jets through detailed planar measurements of the flow velocity in both the axial and tangential directions.

Previous investigations revealed a strong influence of the nozzle angles on the flow characteristics of multiple confined jets[3, 4, 6, 7, 14, 15, 17, 18]. It has been found that the impingement of inclined jets ($\alpha_j > 0°$) generates a merged flow downstream from the jet merging point (P_{mer}), termed the "resulting jet", together with a reverse flow upstream from this, termed the "upstream reverse flow"[4]. It has also been found that an increase in nozzle inclination angle α_j can significantly increase the turbulence intensity and mixing efficiency within jet merging region[3]. Importantly, the Particle Image Velocimetry (PIV) measurements of Long *et al.*[7] identified three distinctive flow regimes generated with the combination of α_j and θ_j for multiple confined jets (See in Fig. 1), which are:

- Regime I: A dominant external recirculation zone (ERZ) surrounding a small central recirculation zone (CRZ);
- Regime II: An upstream ERZ that is of similar extent to the downstream CRZ;
- Regime III: A dominant CRZ downstream from a small upstream ERZ.

Long *et al.*[7] characterized the flow regimes by the relative size and position of the ERZ and CRZ within a cylindrical chamber and assessed their dependence on the geometric configuration of the nozzle and chamber. They found that, for a given value of α_j ($25° \leq \alpha_j \leq 45°$), an increase in θ_j from $5°$ to $15°$ significantly increases the axial extent of the CRZ and reduces the size of the ERZ, leading to the transition from Regime I to Regime III. However, since that study only measured the velocity data in axial plane, the tangential velocity and its corresponding swirling flow within the ERZ and CRZ remains unknown. This gap is significant because the strength of swirl within the large-scale recirculation zone is crucial for achieving desirable mixing and flow stabilization for relevant configurations such as vortex combustors[19, 20], cyclone reactors[21] and solar thermal devices[22, 23]. Hence, there is a need for reliable, comprehensive and sufficient data under well-defined, consistent inflow and boundary conditions to fully characterize the swirl within the ERZ and CRZ that generated by a range of α_j and θ_j.
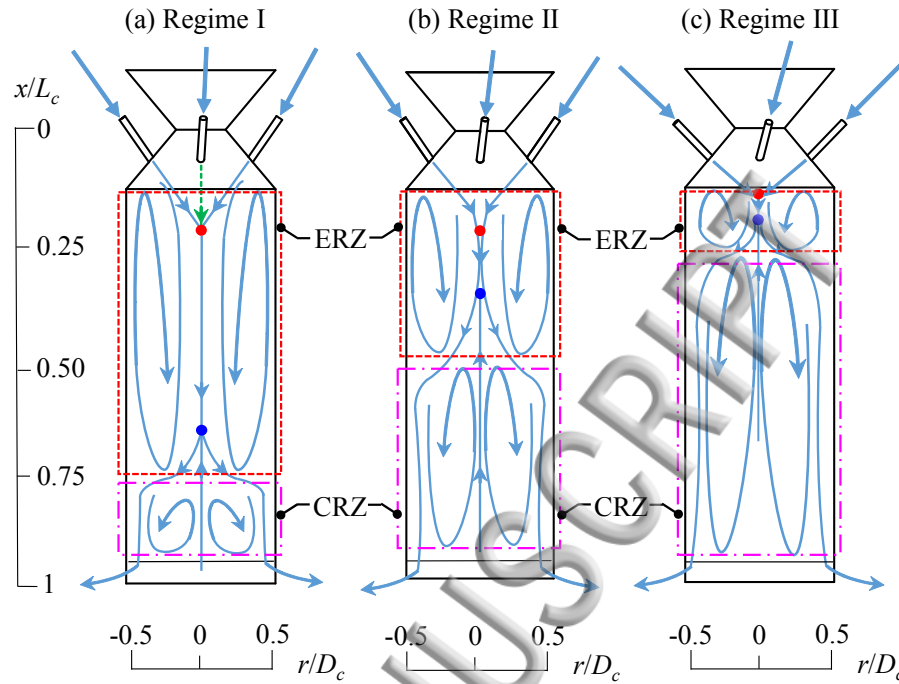
FIG. 1. Schematic diagrams of the three dominant flow regimes within the rotationally symmetric MIJCC configurations, showing the eternal and central recirculation zones (CRZ and ERZ) [adapted from Long *et al.*[7]].

Flow unsteadiness has been widely investigated for swirling annular jets configurations[9, 18, 24-31]. One of the key flow features is the precessing vortex core (PVC) within the recirculation zone, which has been identified for a wide range of vortex applications[27, 29, 30, 32]. The PVC is a large-scale coherent and time-dependent flow structure embedded within a vortex, which is defined as the precession of the vortex-core relative to the geometric axis of an axisymmetric device, as described in the detailed review by Syred[9]. Their study showed that the PVC can significantly influence flow behavior, mixing performance and combustion efficiency for vortex devices such as cyclones and swirl burners. Previous investigations revealed that the presence of the PVC depends strongly on the geometric confinement[33], recirculation zone[34] and thermal conditions[28, 35]. Consistent with this, our previous PIV measurements showed that the strong interaction between multiple-jets tends to amplify flow precession and oscillation[6, 7], although this has not yet been quantified. However, while the dynamics of the PVC in a swirling or single jet has been widely docmented[9], none of the previous investigations provided a comprehensive understanding of the influence of the multiple confined jets on the PVC, so that the dependence of the PVC on large-scale recirculation zones generated by multiple-jets remains unclear. Hence, there is also a need to better understand the characteristics of the PVC generated by multiple jets within a confined environment.

In light of the needs identified above, the overall objective of the present study is to provide new understanding of the swirling and precessing flows generated within the MIJCC. The specific aims are as follows: (a) to provide a quantitative description of the mean and root-mean-square (RMS) flow-fields in both the axial and tangential directions for multiple confined jets; (b) to identify the characteristics of swirl within the ERZ and CRZ generated by a confined chamber

3

with multiple-jets; and (c) to characterize the dependence of the precessing vortex core (PVC) on the configuration of the four confined jets.

II. METHODOLOGY

A. Configurations selected in the present study

A schematic diagram of the MIJCC device, which has been described in detail in our previous work[7], is presented in Fig. 2. Briefly, the MIJCC consists of a cylindrical chamber with a conical expansion, a secondary concentrator (SC) and a number $N_j = 4$ of rotationally-symmetric inlet jets. The inlet jets were distributed around the conical expansion of the main cavity with a combination of α_j and θ_j. The SC was closed at the largest end to prevent flow to or from the ambient environment (labelled with a red line), while the flow leaves the device through an annular outlet around a bluff end-wall (labelled with a blue enclosure). In addition, the cylindrical section of the MIJCC was manufactured from transparent acrylic to enable optical access into the chamber. The key geometric parameters of the MIJCC investigated in the present experiment are given in Table I.

Two azimuthal ($\theta_j = 5°$ and $15°$) and inclination angles ($\alpha_j = 25°$ and $45°$) were chosen to generate three experimental configurations of the MIJCC representing Regimes I, II and III in Fig.1. These angles have been selected to ensure that each distinctive class of flow-feature (i.e., each flow regime) is represented, based on our previous work[6-8]. A detailed description of the experimental cases is presented in Table II.
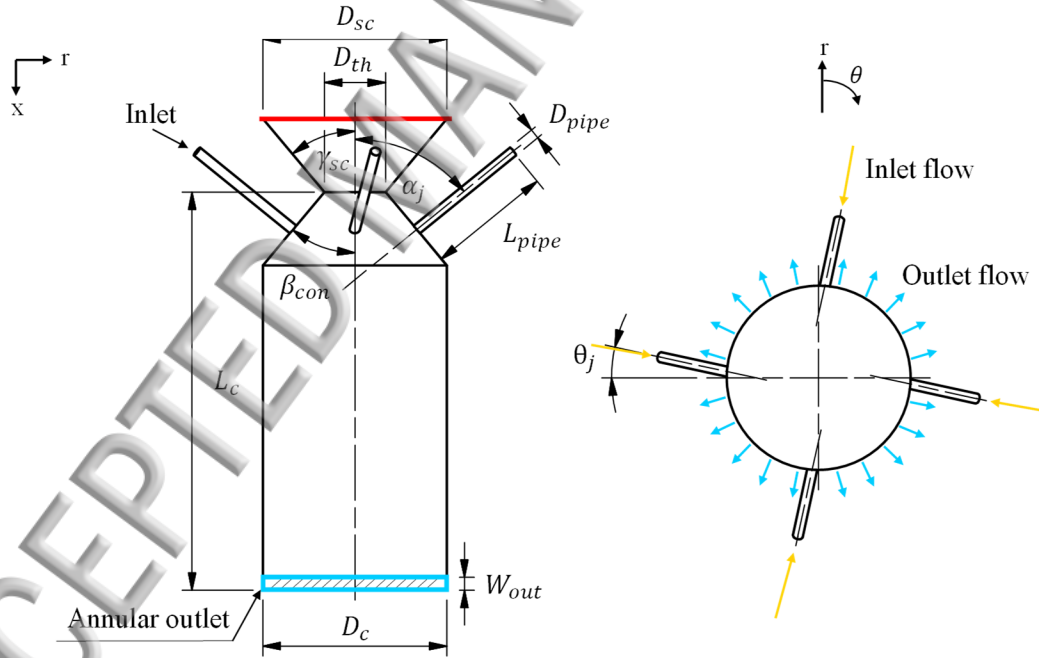

FIG. 2. Schematic diagram of the Multiple Impinging Jets in a Cylindrical Chamber (MIJCC) configurations investigated here, showing the key geometric features from the axial cross section (left) and a radial cross section (right). Here the plane of the movable flap and that of the annular outlet are highlighted with red line and blue enclosure, respectively.

TABLE I. Values of the geometric parameters of the MIJCC (see Fig.1) that have been investigated in the present study.

Dimensions	Description	Value
D_c	Chamber Diameter (mm)	74
D_{sc}	Diameter of the Secondary Concentrator (mm)	74
D_{th}	Throat Diameter (mm)	24.6
D_{pipe}	Inlet Pipe Diameter (mm)	3.35
L_c	Chamber Length (mm)	225
L_{pipe}	Inlet Pipe Length (mm)	150
W_{out}	Annular Outlet Gap (mm)	3
β_{con}	Conical Expansion Angle (degree)	40°
γ_{sc}	Angle of the Secondary Concentrator (degree)	40°

TABLE II. The notation for the MIJCC configurations investigated in the present study.

Experiment Case No.	Configurations	Inclination angles, α_j	Azimuthal angles, θ_j	Flow Regime
1	MIJCC-25-05	25°	5°	I
2	MIJCC-25-15	25°	15°	II
3	MIJCC-45-15	45°	15°	III

B. Measurements

The optical arrangements were similar to those reported previously[6, 7], so that only the key details are described here. The flow-field was measured using PIV. The working fluid was water at ambient temperature, which avoids the deposition of seeding particles onto the confining walls. The jet Reynolds number $Re_D = \rho_f U_e D_{pipe}/\mu_f = 10{,}500$ (where ρ_f is the fluid density and μ_f is the fluid dynamic viscosity) ensures that the flow at the nozzle exit is in the fully turbulent regime. The flow was seeded with hollow glass spheres with a specific gravity of 1.1 and a particle diameter of 12 μm. A closed-loop system, including a water pump (Pan World NH-200PS), a frequency converter (Danfoss VLT 2800) and flowmeters (ABB D10A11), was used to recirculate the water from the outlets of the tank to the inlet-pipes. Importantly, a symmetrical manifold system which consists of two straight pipes and four gently-curved flexible pipes ($L_{pipe}/D_{pipe} \approx$ 196), ensures a fully developed pipe flow is achieved at the exit plane of the supply pipes[36].

Figure 3 presents the optical arrangement and the measurement regions for the present study. A double-head Nd:YAG laser (Quantel Brilliant B) was used to generate a light sheet of 1.5 mm thickness with a combination of three cylindrical lenses (Thorlabs). A Charged Coupled Device (CCD) camera (Kodak Megaplus ES2093) was used to capture the PIV images for each measurement. The image size was selected so that it spans the entire radial cross-section of the cylinder ($D_c = 74$ mm).

The measurement planes for the present study are listed in Table III. Five radial planes (orthogonal to the axis) and one axial plane (across the axis) within the cylindrical chamber of the MIJCC were assessed. It should be noted that the results for cases 1 and 6 are only reported for selected figures for conciseness because they are qualitatively similar to those from other planes.

5

The selection of these measurement planes ensures that the velocity data can be obtained from all three classes of flow (see Table III for details).

A minimum of 1500 PIV image pairs were recorded by the CCD camera for each measurement. The raw images were processed utilizing an in-house PIV code in MATLAB R2015a (Mathworks), employing a multi-grid correlation algorithm with 50% overlap to calculate the displacement of tracer particles and also to minimize noise. In addition, an in-house post-processing PIV code was used to identify the outliers (erroneous vectors) for all experimental conditions. As a result, the average number of outliers was less than approximately 5% of the total vectors, and all outliers were removed from the ensemble. The details of the key experimental parameters are listed in Table IV.

The overall uncertainty associated with the PIV measurements was assessed via a series of systematic analysis steps. The estimated uncertainty derived from the experimental apparatus (i.e., flowmeter, water pump and frequency converter) was measured to be less than 2%, while the uncertainty of a given measurement position was estimated to be $\pm$ 0.05 mm within the measurement region. The experimental errors associated with the laser system (e.g., time-delay) were estimated to be less than 2%. Also, the uncertainty contributed from the image sample size was calculated to be less than 1%. On this basis, the overall uncertainty of the measured mean and RMS velocities for the present PIV measurements was estimated to be approximately 5%.
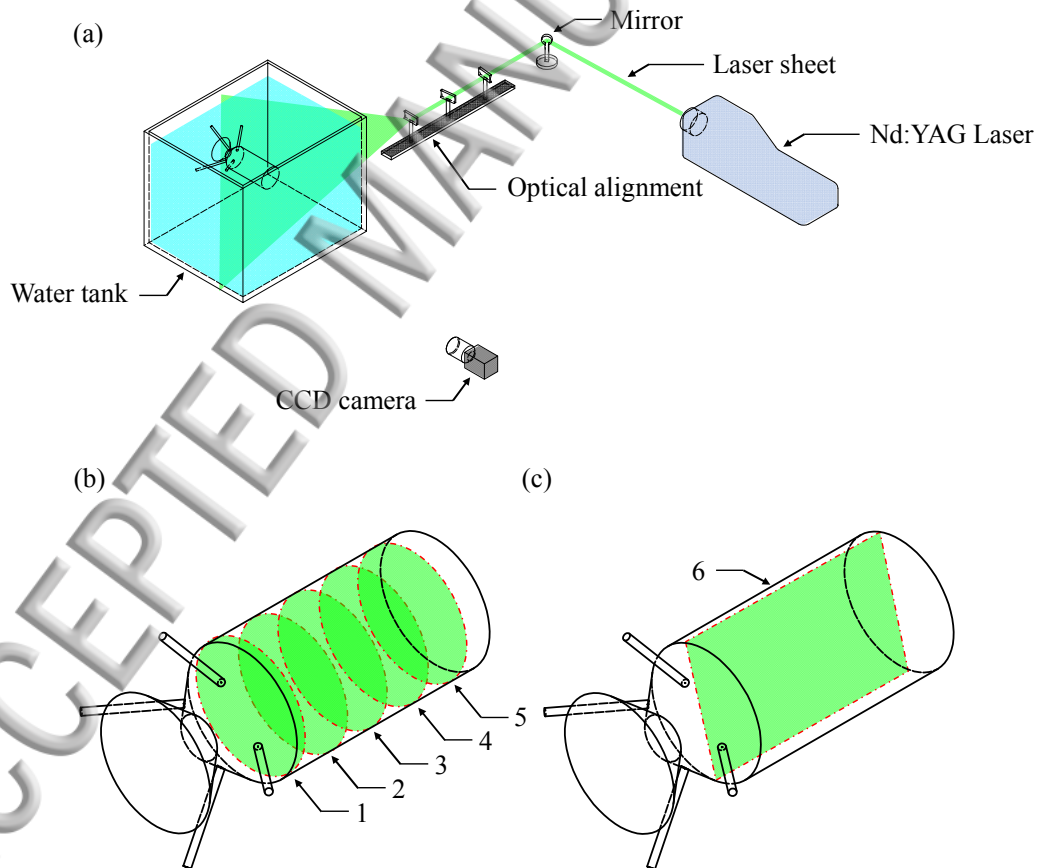

FIG. 3. (a) Schematic diagram of the optical arrangment, showing the laser, optics, light sheet and the water tank (b) the five radial measurement planes, undertaken seperately, along the axis of the MIJCC and (c) the axial measurement plane relative to the chamber.

6

TABLE III. Axial positions of the measurement profiles for which data are reported. The circumferential plane is shown in Fig. 3. Note that the plane 6 denotes the axial plane illustrated in Fig. 3(c).

Measurement plane	Location, x/L_c	Regime I	Regime II	Regime III
1	0.27	ERZ	ERZ	CRZ
2	0.36	ERZ	ERZ	CRZ
3	0.45	ERZ	CRZ	CRZ
4	0.63	ERZ	CRZ	CRZ
5	0.80	CRZ	CRZ	CRZ
6	N/A	ERZ & CRZ	ERZ & CRZ	ERZ & CRZ

TABLE IV. Details of the key experimental parameters for the present PIV measurements.

Experimental parameters	Value
Bulk mean velocity at nozzle exit, U_e (m/s)	2.8
Inlet Reynolds number, Re_D	10,500
Laser wavelength (nm)	532
Laser thickness (mm)	1.5
Laser frequency (Hz)	10
Camera array size (pixels)	1920×1080
Measurement region (mm)	134×77
Particle Stokes number, Sk_D	0.003
Image bit depth (bit)	12
Spatial resolution (mm)	$2 \times 2 \times 1.5$
Interrogation window (pixels)	32×32

III. RESULTS AND DISCUSSION

A. Mean velocity fields

Figure 4 presents the contours of mean tangential velocity (U_θ), normalized by the nozzle exit velocity (U_e), labelled with arrows to indicate flow direction (black arrows), and magnitude (both the length of the arrows and the color map) at four radial planes x/L_c = 0.36, 0.45, 0.63 and 0.80 for the configurations of [Figs. 4(a) – 4(d)]: Regime I ($\alpha_j = 25°$ and $\theta_j = 5°$), [Figs. 4(e) – 4(h)]: Regime II ($\alpha_j = 25°$ and $\theta_j = 15°$), and [Figs. 4(i) – 4(l)]: Regime III ($\alpha_j = 45°$ and $\theta_j = 15°$). The locations of the CRZ and ERZ for each plane are also presented.

For the case of Regime I (dominant ERZ and small CRZ), the mean flow spirals outward from the center to the near-wall region in each case (except for the most downstream one), with a magnitude that is greatest at x/L_c = 0.36 and decreases with axial distance $x/L_c \geq 0.45$. It can also be seen from the color scale that there is a trend for the magnitude of U_θ within the outer regions of the chamber (i.e., within the ERZ) to decrease with axial distance from x/L_c = 0.36 to x/L_c = 0.63. In contrast, the magnitude of U_θ near to the axis (i.e., within the CRZ) remains almost independent of axial distance. This is qualitatively similar to the velocity field generated by annular swirling jets[37]. Taken together, it can be concluded that the swirl intensity within the ERZ decreases with an increase in x/L_c within this regime.

7

For Regime II (where the ERZ and CRZ are of similar size), the velocity contours show that the distribution of U_θ is almost independent of axial distance, so that it is higher than that of Regime I, for all cases of x/L_c. This confirms that the axial extent of the swirl zone is greater in Regime II than in Regime I. The contours also show that the distribution of U_θ does not change significantly from the upstream ERZ ($x/L_c = 0.36$) to the downstream CRZ planes ($x/L_c \geq 0.45$). This confirms that the decay of swirl within the chamber reduces as the size of the CRZ is increased, as expected. In addition, it should also be noted that at each axial position, the value of U_θ is fairly uniform, except for a lower velocity component near to the axis. This also suggests that the symmetry of the tangential velocity tends to be approximately achieved in this regime.

Regime III is characterized by a generally significantly higher magnitude of U_θ than the other regimes, as can be seen from the redder color, consistent with the greater swirl angle of the inlet jets. Indeed, the flow direction approaches a tangential direction except for the very core. In addition, the distribution of U_θ is relatively uniform for all locations considered here. That is, the swirl generated with the multiple inlet-jets is almost independent from the location of radial plane for Regime III. This is consistent with the dominance of the CRZ throughout all measured planes. It can also be seen that a high velocity region ($U_\theta/U_e \approx 0.12$) occurs within the range $-0.15 \leq r/D_c \leq 0.15$ for all measured locations except the central point ($r/D_c \approx 0.15$). This, in turn, suggests that a higher degree of swirl occurs close to the axis of the cylindrical chamber[29], while this pronounced swirl region is not observed in the other two regimes. Hence, it can be concluded that the significance of the swirl within the central region tends to increase significantly as the dominant flow feature changes from the ERZ (Regime I) to the CRZ (Regime III).

It is also worth noting that, for a given radial plane x/L_c, the magnitude of tangential velocity U_θ typically increases from Regime I to Regime III, with the highest value of U_θ for each plane is measured from Regime III. For example, the swirl at $x/L_c = 0.80$ in Regime III [Fig. 4(l)] is an order of magnitude higher than that in Regime I [Fig. 4(d)]. This also indicates that the combination of high inclination and azimuthal angles ($\alpha_j = 45°$ and $\theta_j = 15°$) tends to significantly increase the degree of swirl at any given location for multiple confined jets.

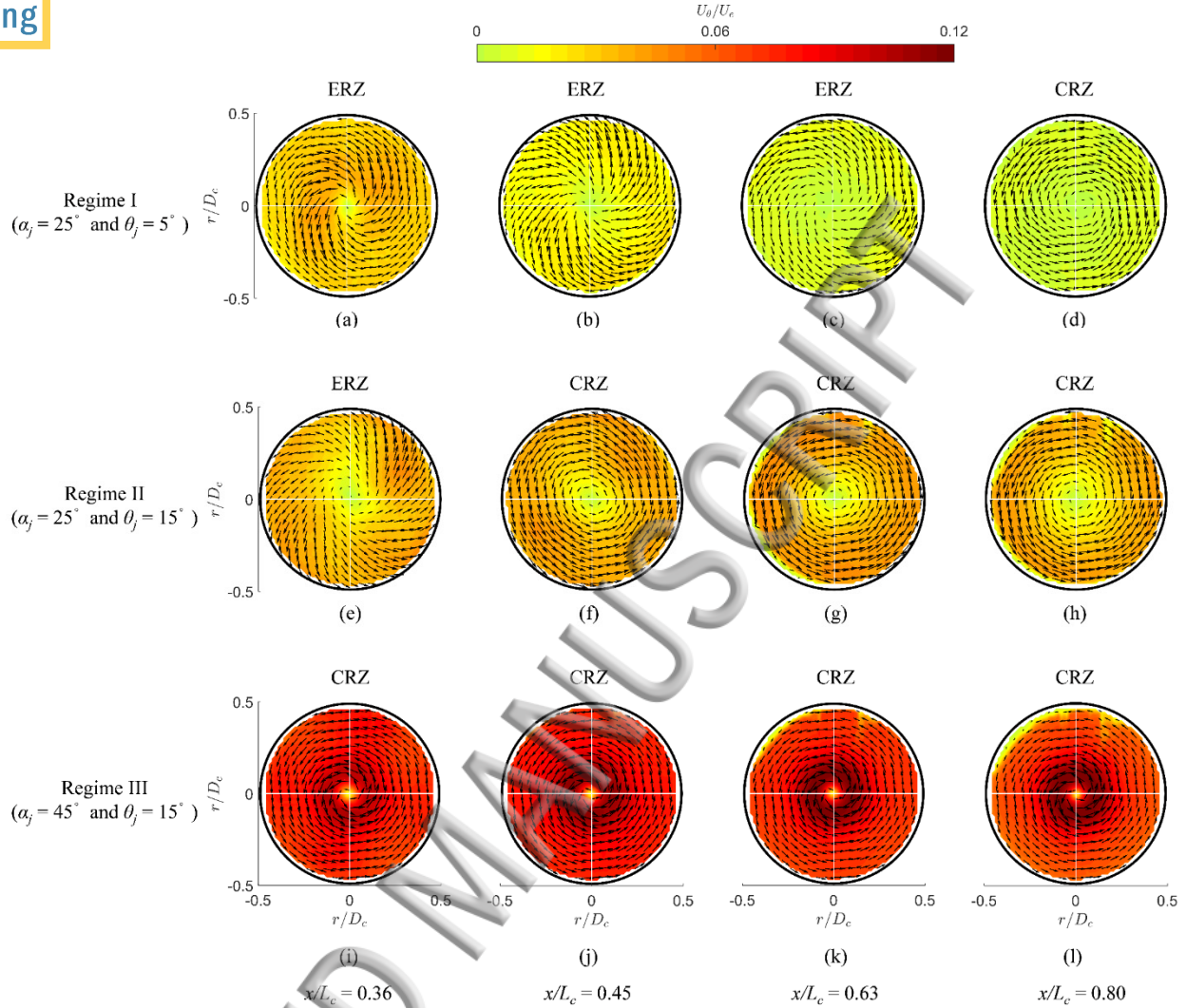FIG. 4. Mean tangential velocity (U_θ) normalized by the nozzle exit velocity (U_e), labelled with arrows to indicate flow direction (black arrows) and magnitude (color map) at four axial planes x/L_c = 0.36, 0.45, 0.63 and 0.80 within the MIJCC for the configurations of [(a) – (d)]: Regime I ($\alpha_j = 25°$ and $\theta_j = 5°$), [(e)-(h)]: Regime II ($\alpha_j = 25°$ and $\theta_j = 15°$) and [(i)-(l)]: Regime III ($\alpha_j = 45°$ and $\theta_j = 15°$). Note that the axes and pseudo color-scales are identical for all cases.

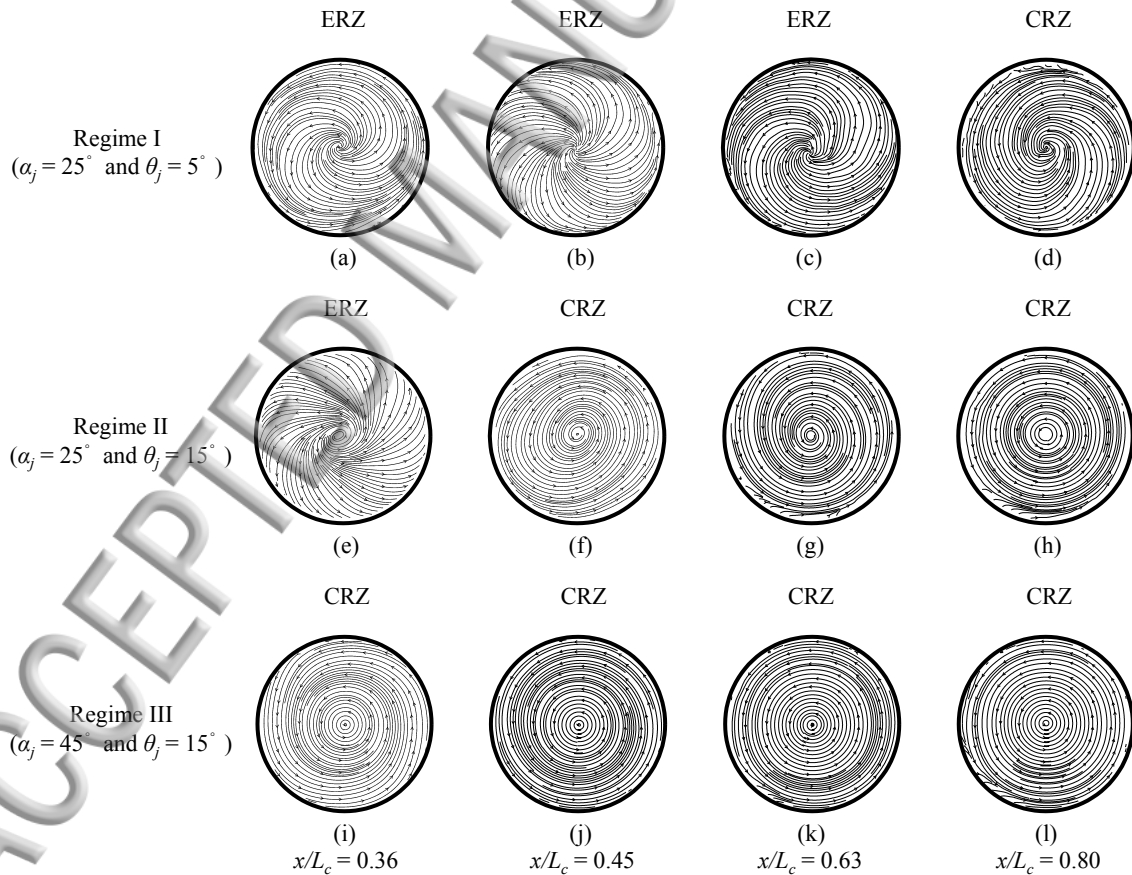Figure 5 presents the measured streamlines, labelled with arrows to indicate the flow direction at four radial planes x/L_c = 0.36, 0.45, 0.63 and 0.80 for all experimental conditions. Clear differences can be seen. For the case of Regime I [Figs. 5(a) – 5(d)], it can be seen that the flow exhibits an outwardly spiraling flow pattern from a point source at the cylinder axis within three planes in the ERZ, i.e., x/L_c = 0.36, 0.45 and 0.63. This flow is generated by the central resulting jet formed by the merging of the inlet jets, superimposed onto the swirl generated by the tangential component of the inlet-jets ($\theta_j = 5°$). This flow pattern is consistent with conventional swirling jets[38, 39] and also with our previous paper[7]. However, further downstream at x/L_c =0.80, the flow exhibits an internally spiraling flow towards the axis within the CRZ (i.e., the source becomes a sink), while the swirling direction unchanged. This flow pattern is caused by the low-pressure core with the CRZ, which also generates the reverse flow zone.

9

For the case of Regime II [Figs. 5(e) – 5(h)], the trends are similar although the axial extent of each region changes. The spiraling out from the source on the axis is only present at location x/L_c = 0.36, which corresponds well with the presence of the ERZ. The other two positions exhibit a sink at the axis x/L_c = 0.45 and 0.63, corresponding well with the CRZ. Importantly, as the radial component becomes weaker for x/L_c = 0.80, the flow approaches being tangential. This indicates that a strongly swirled flow is present in which the tangential velocity U_θ is much greater than the radial velocity component (U_r).

For the case of Regime III [Figs. 5(i) – 5(l)], the flow-field everywhere is characterized by a very weak radial inflow, so that it approaches an almost purely rotational flow for all radial planes investigated here. This is consistent with the presence of highly-swirled flow for Regime III, together with a dominant CRZ.

Overall, the results show that, a source within the rotational flow is associated with the presence of an ERZ, while a sink within the rotational flow represents the occurrence of a CRZ. This is consistent with expectation. Importantly, as the source or sink is absent and a flow of pure rotation occurs, the region tends to be dominated by a high-swirled flow within the CRZ (for which $U_\theta > U_r$). That is, the value of swirl angles (α_j and θ_j) and their corresponding large-scale recirculation zones (ERZ and CRZ) have a controlling influence on the presence of rotational flow patterns for multiple confined jets.

FIG. 5. Measured streamlines, labelled with arrows to indicate the flow direction at four axial planes x/L_c = 0.36, 0.45, 0.63 and 0.80 within the MIJCC for the configurations of [(a) – (d)]: Regime I, [(e)-(h)]: Regime II and [(i)-(l)]: Regime III.

Figure 6 presents the radial profiles of the normalized mean tangential velocities (U_θ/U_e) at four radial planes $x/L_c = 0.36$, 0.45, 0.63 and 0.80 within the MIJCC chamber for all experimental conditions. Note that the axes and symbols are identical for all of these sub-figures. The measurements for Regime I [Fig. 6(a)] show that the magnitude of U_θ/U_e decreases by approximately 70% as x/L_c is increased from 0.36 to 0.8. For example, the peak velocity, $(U_\theta/U_e)_{max}$, decreases from 0.03 at $x/L_c = 0.36$ to 0.01 at $x/L_c = 0.8$. Furthermore, the value of U_θ/U_e decreases faster within the ERZ than that in CRZ plane. For example, it decreases by 70% from $x/L_c = 0.36$ to 0.63 (ERZ) and only by 10% from $x/L_c = 0.63$ to 0.80 (CRZ). It should also be noted that the magnitude of the tangential velocity $U_\theta \approx 0.01U_e$ to $0.03U_e$ for all measured planes in Regime I. This is an order of magnitude lower than that of the axial velocity ($U_x \approx 0.15U_e$) as we reported previously[7]. Hence, the swirl in Regime I is weak.

For Regime II [Fig. 6(b)], it can be seen that the tangential velocity does not change as significantly with x/L_c as it does in Regime I, but only decays by about 30% from upstream ($x/L_c = 0.36$) to downstream ($x/L_c = 0.80$). The decay of the tangential velocity is noticeably lower than that of Regime I as $(U_\theta/U_e)_{max}$ at $x/L_c = 0.80$ is approximately 40% higher than that for the case of $\theta_j = 5°$ (within the CRZ). This reveals that the swirl increases as θ_j is increased, as expected. It can also be seen that the radial profile of U_θ/U_e increases monotonically with the radial distance (r) from the axis to $r/D_c \approx 0.25$ for $x/L_c = 0.36$ and 0.45, plateaus and then increases slightly toward the wall. This is qualitatively consistent with a turbulent swirling pipe flow measured by Kitoh[40] [see the inset of Fig. 6(b)], which indicates that the flow is characterized by a forced vortex within these planes. However, the magnitude of the forced vortex in Regime II is approximately 80% lower than that of Kitoh[40], indicating that the swirl is weaker in this case. For further downstream planes ($x/L_c = 0.63$ and 0.80), a significant reduction of U_θ/U_e was measured at the near-wall region of $r/D_c \geq 0.46$ ($\approx 10\%$ of the total radius). This implies the transition between a forced and a free vortex, corresponding well with the ERZ and CRZ regions of Regime II.

For Regime III [Fig. 6(c)], the tangential velocity is the highest [$(U_\theta/U_e)_{max} \approx 0.12$]. For all radial profiles, the value of U_θ/U_e increases from 0 to 0.12 within $0 \leq r/D_c \leq 0.15$ and then decreases to 0.07 for $r/D_c > 0.15$. This is qualitatively similar to the PIV data reported by Chinnici et al.[29] for multiple swirling jets, which shows the presence of a forced vortex near to the central region, surrounded by a free vortex, i.e., a "Rankine" vortex (forced and free combined vortex). This vortex has also been widely documented for high-swirled jet configurations[41-44]. Importantly, the combination of a forced and free vortex (Rankine vortex) is typically associated with the presence of a high degree of flow oscillations within the CRZ, such as a PVC[9, 34].

The results in Fig. 6(c) also show that U_θ/U_e in Regime III is around 20% higher than the data of Chinnici et al.[29]. This indicates the presence of a highly-swirled flow for this regime. However, as x/L_c is increased from 0.36 to 0.8, the tangential velocity increases by 10% within the forced vortex ($|r/D_c| \leq 0.15$) while it decreases by 15% within the free vortex ($|r/D_c| > 0.15$). This reveals that the intensity of "Rankine" vortex is not consistent throughout the chamber, although the difference of U_θ/U_e is typically small ($\leq 15\%$).

It is also worth noting that, for the cases where the inclination and azimuthal angles (α_j and θ_j) are both small and an ERZ dominates the chamber (Regime I), the magnitude of tangential velocity decreases significantly (by 40%) with x/L_c, while for the cases in which both α_j and θ_j are sufficiently large to generate a dominant CRZ (Regime III), the decay in the tangential velocity is relatively small (by up to 15%) and the magnitude remains the highest. This suggests that the strength of the swirl persists further within a CRZ than within an ERZ.
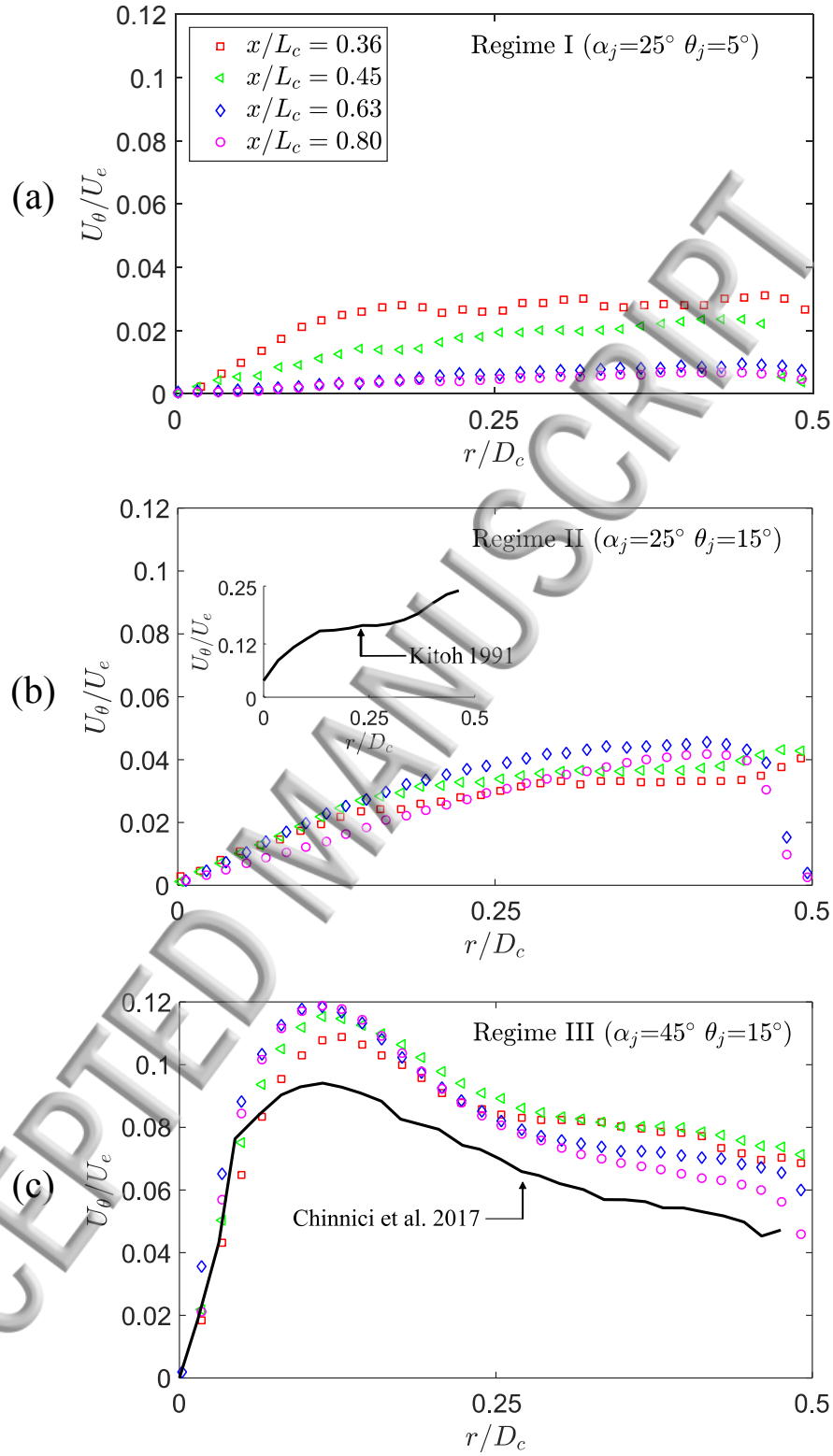
11

FIG. 6. Radial profiles of the normalized mean tangential velocities (U_θ/U_e) at four radial planes x/L_c = 0.36, 0.45, 0.63 and 0.80 within the MIJCC for cases of (a): Regime I, (b): Regime II and (c): Regime III. Note that the axes and symbols are identical for all cases.

B. RMS of the turbulent flow fields

Figure 7 presents the radial profiles of normalized tangential RMS (root-mean-square) velocity (u'_θ/U_e) within the MIJCC chamber at four radial planes x/L_c = 0.36, 0.45, 0.63 and 0.80 for the configurations of (a) Regime I (α_j = 25° and θ_j = 5°), (b) Regime II (α_j = 25° and θ_j = 15°) and (c) Regime III (α_j = 45° and θ_j = 15°).

For Regime I [Fig. 7(a)] the location of the peak RMS velocity, $(u'_\theta/U_e)_{max}$, at x/L_c = 0.36 and 0.45 is found at, or close to, the centre of the chamber, and then decreases approximately linearly towards the wall region. A maximum in turbulent fluctuation within the central region is associated with the unsteady merging point of the multiple inlet-jets[7], resulting in a precessing jet flow[9]. At x/L_c = 0.63, the RMS velocity is 70% lower than at x/L_c = 0.45, while the radial profile of the RMS velocity remains approximately constant ($u'_\theta/U_e \approx 0.025$) across the chamber's radius. The value of u'_θ/U_e continues to decrease with axial distance to a value of $u'_\theta/U_e \approx 0.02$ at x/L_c = 0.80, which is very close to uniform throughout the radial profile. Taken together, it can be concluded that the fluctuations in the tangential velocity for Regime I reduces significantly with axial distance from the nozzle exit, consistent with trends in conventional annular jets[14, 37].

It can be seen from Fig. 7(b) that the tangential RMS velocity in Regime II is significantly lower than that of Regime I at x/L_c = 0.36 and 0.45. However, u'_θ/U_e is quite similar in the two regimes at x/L_c = 0.63 and 0.80. This gives some evidence that the fluctuation in tangential velocity tends to reduce as θ_j is increased. The shapes of the upstream profiles are also different. At the two upstream locations, x/L_c = 0.36 and 0.45, the RMS peaks on the axis for Regime I, but peaks away from the axis for Regime II. However, further downstream they are flatter. This indicates that the axial extent of the zone with relatively low fluctuation of swirl in the downstream region grows from Regime I to Regime II. Hence, it can be concluded that the radial profile of the RMS of tangential velocity is small and relatively flat for the CRZ region, but significantly higher for the ERZ.

For Regime III [Fig. 7(c)] where the flow is characterized by a dominant CRZ, it can be seen that a pronounced peak in u'_θ/U_e occurs at the central region $-0.15 \leq r/D_c \leq 0.15$ for all radial profiles, with the peak value of $u'_\theta/U_e \approx 0.06$ occurring at the centerline of the chamber. This corresponds well with the maximum gradient of the mean tangential velocity (U_θ) shown in Fig. 6(c). That is, a high value of u'_θ/U_e is associated with the central region for Regime III. Such a large fluctuation in the tangential velocity is commonly associated with a high degree of flow unsteadiness, which may be evidence of the presence of a PVC within the central region, consistent with previous studies in swirled burners and reactors[9, 13, 37, 45]. Importantly, this pronounced peak only occurs at Regime III, which suggests that this regime is most likely to generate a PVC at, or close to, the axis of the chamber.

Overall, it can be concluded that, firstly, for a given value of nozzle angle (α_j and θ_j), the degree of fluctuation in the tangential velocity decreases along the axis of the chamber for both the ERZ and CRZ, although the reduction is most significant for the smallest jet angles considered here (Regime I) and, secondly, an increase in α_j and θ_j (Regime III) leads to a significant increase in the velocity fluctuation of the central region ($r/D_c \approx 0$) for a given radial plane (x/L_c). This also highlights the influence of the CRZ on the amplification of flow unsteadiness along the axis of the chamber, as discussed in previous study[7].
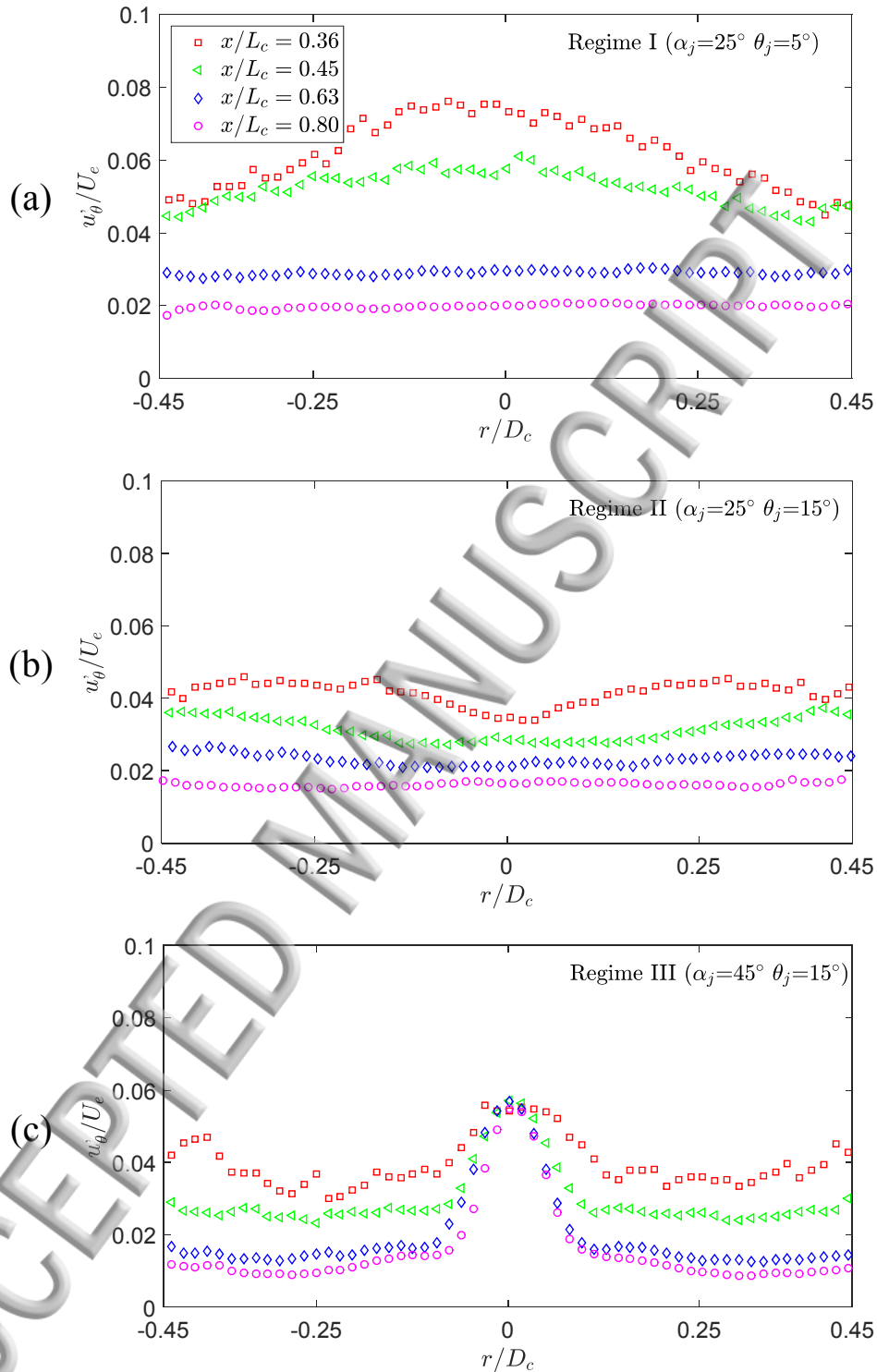
FIG. 7. Radial profiles of tangential RMS (root-mean-square) velocity normalized by the nozzle mean exit velocity (u'_θ/U_e) at four radial planes x/L_c = 0.36, 0.45, 0.63 and 0.80 within the MIJCC for configurations of (a): Regime I (b): Regime II and (c): Regime III. Note that the axes and symbols are identical for all cases.

14

Figure 8 presents axial profiles of the evolution of normalized axial (u'_x/U_e) and radial RMS velocities (u'_r/U_e), along the centerline of the MIJCC chamber for representative configurations that generate Regimes I, II and III. The data for Regimes I and II are reproduced from our previous paper (Long *et al.*[8]) to complete the data set, while red solid line denotes Regime I and blue dashed-line refers to Regime II. For Fig. 8(a), the results show that the transition from Regime I to Regime III leads to a significant decrease in axial RMS velocity u'_x along the axis of the chamber. The magnitude of the peak $(u'_x/U_e)_{max}$ remains almost constant ($u'_x/U_e \approx 0.1$) from Regime I to Regime II and decreases by 40% from Regime II to Regime III. The position of the peak also moves upstream from $x/L_c \approx 0.32$ (Regime I) to 0.15 (Regime III). This is consistent with the upstream movement of the jet merging point for each case, as reported previously[7]. The axial extent of the region with low u'_x/U_e therefore increases commensurately from Regime I, where it is negligible, to Regime III, where it is the dominant phenomena in the measured region. Hence, it can be concluded that Regime III is associated with a lower fluctuation in the axial velocity component along the centerline of the chamber.

The axial profile of u'_r/U_e is presented in Fig. 8(b). It can be seen that, for Regime I and II the position of the peak tends to be further upstream than for u'_x/U_e and the corresponding axial extent is shorter. Hence the average value of u'_r/U_e in Regime II is typically 30% lower than that in Regime I. However, the peak for Regime III is found further upstream and asymptotes to a higher value of $u'_r/U_e \approx 0.06$ than for the other regimes. This value of $u'_r/U_e \approx 0.06$ is similar to that of the pronounced peak in u'_θ within the central region of the radial planes reported above. Taken together, it can be concluded that Regime III is associated with strong fluctuation in the radial and tangential velocity components, but weaker fluctuations in the axial direction which is also consistent with the presence of precessing flows for the configurations with high nozzle angles ($\alpha_j = 45°$ and $\theta_j = 15°$).
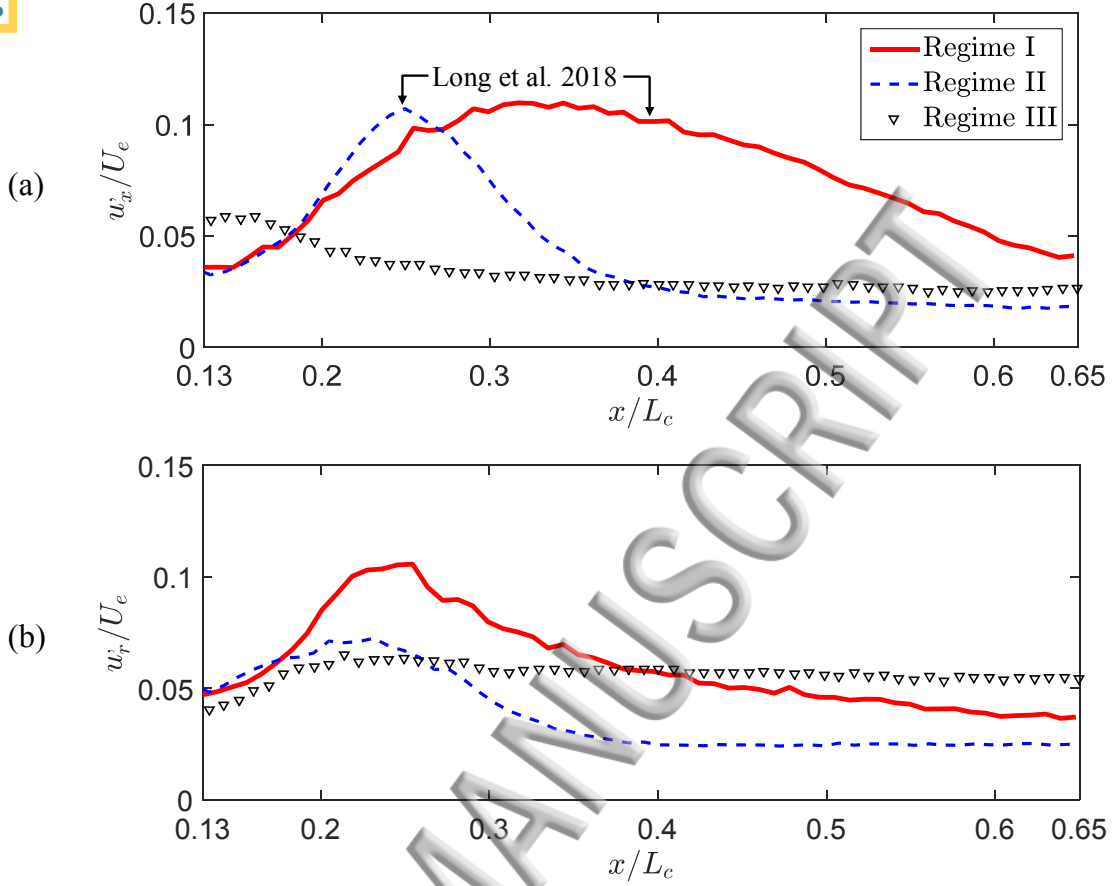
FIG. 8. Evolution of (a) normalized axial RMS (u'_x/U_e) and (b) normalized radial RMS velocity (u'_r/U_e) along the centerline of the MIJCC for all experimental cases. The red and blue lines denote the data published in our previous work (Long et al. 2018). For clarity, only every second data point is presented and both cases use identical axes and symbols.

C. Characterization of the precessing vortex core

Figure 9 presents (a) two typical instantaneous streamlines, labelled with arrows to indicate flow direction, and (b) the angular displacement of the vortex-core relative to the center of the cylinder (θ_{core}), as a function of time (t) for the case of Regime III ($\alpha_j = 45°$ and $\theta_j = 15°$). Note that the data are presented only at $x/L_c = 0.8$ here for consistency. The location of the vortex-core was determined by a combination of mathematical calculations and visual observation. Mathematically, the position of the vortex-core is defined as the crossing point where the tangential velocity U_θ and the radial velocity U_r equals, or approaches zero on the θ-r coordinate system, following Grosjean et al.[26] and Volkert et al.[46]. The results were calibrated with the visualization from the raw PIV images to obtain the final location of the vortex-cores. On this basis, the uncertainty of the vortex-core location was estimated to be less than 10%.

For the instantaneous velocity field [Fig. 9(a)], it can be seen that the vortex-core (labelled with a red cross) moves from the bottom-half [Fig. 9(a) left] to the top-half [Fig. 9(a) right] section of the cylindrical chamber, with a significant displacement relative to the axis of the chamber (labelled with the red lines). That is, the location of vortex-core changes significantly with time. The temporal displacement of the vortex-core is presented in a time-series in Fig. 9(b) for some

16

cycles. This shows that θ_{core} moves periodically around the axis of the chamber with a regular frequency. This is a typical of previous descriptions of a PVC[9, 29], which confirms its presence within the cylindrical chamber.

(a)

(b)
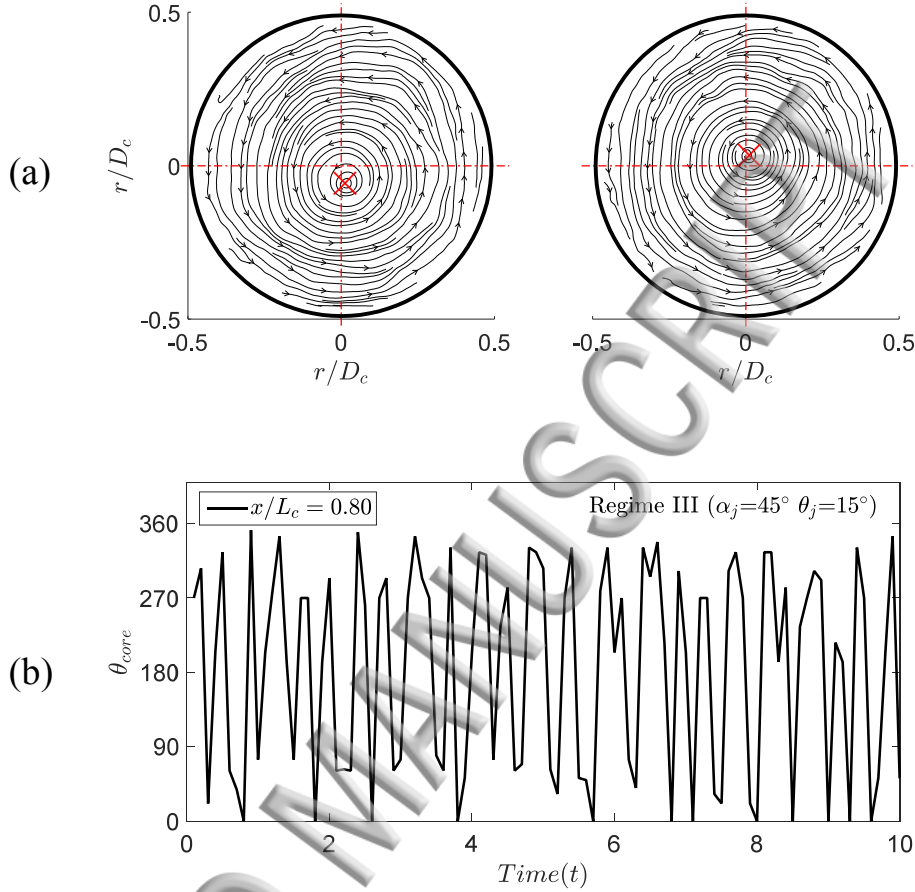
FIG. 9. (a) Typical instantaneous streamlines, labelled with arrows to indicate the flow direction for the case of $\alpha_j = 45°$ and $\theta_j = 15°$ (Regime III) at the plane $x/L_c = 0.8$, and (b) the angular displacement of the vortex-core (θ_{core}) as a function of the time (t).

Figure 10 presents the probability density function (PDF) of the radial displacement of the vortex-core relative to the axis of the chamber (r_{core}), normalized by the chamber diameter (D_c) for the cases of Regimes I, II and III. All of these data are measured in the CRZ at the radial plane $x/L_c = 0.8$ (refer to Table III). The results show that the most probable displacement of the vortex-core is $r_{core}/D_c \approx 0.11$ to 0.13 for Regimes I and II, while it is smaller at $r_{core}/D_c \approx 0.03$ for Regime III. However, the peak in probability is much sharper for Regime III, showing that the fluctuations are more regular. The finding that the transition between Regime I and Regime II does not significant influence the radial displacement of the PVC is consistent with them both being associated with a dominant ERZ upstream from $x/L_c = 0.8$, while Regime III is associated with a CRZ that fills almost the entire cylindrical chamber. Hence, the presence of a dominant CRZ tends to inhibit the precession of vortex-core and to generate a coherent PVC for the configurations of multiple confined jets.

It can also be seen from Fig. 10 that the higher peak in the PDF for Regime III is consistent with the higher values of RMS velocities along the centerline of the chamber for Regime III (see also Fig. 7 and Fig. 8). Taken together, it can be concluded that the PVC is present in all of these

17

flows, regardless the types of vortex (i.e., free, forced or Rankine), although it is more coherent in the CRZ of Regime III, but with a smaller displacement than it is for Regime I.
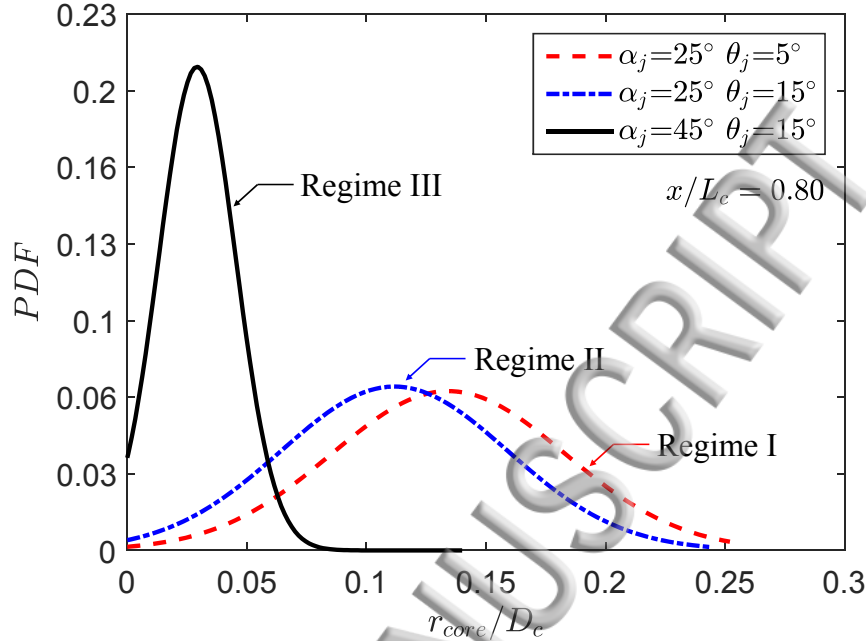
FIG. 10. Probability distribution of the radial displacements of the vortex core relative to the axis of the chamber, normalized by the chamber diameter, for the configurations of Regime I ($\alpha_j = 25°$ and $\theta_j = 5°$), Regime II ($\alpha_j = 25°$ and $\theta_j = 15°$) and Regime III ($\alpha_j = 45°$ and $\theta_j = 15°$).

Figure 11 presents the averaged radial displacement of the vortex-core ($\bar{r}_{core}$) normalized by the chamber diameter (D_c), at five radial planes (x/L_c = 0.27, 0.36, 0.45, 0.63 and 0.80) for the configurations generating Regimes I, II and III. Data are only presented for those cases where a vortex-core can be identified from the method illustrated by Fig. 9. It can be seen that the axial extent of the regions in which a PVC can be identified is greatest for Regime III (x/L_c = 0.27, 0.36, 0.45, 0.63 and 0.80) and least for Regime I (x/L_c = 0.80). This is consistent with the increase in the magnitude of the tangential velocity for Regime III. Furthermore, these regions correspond to radial planes where a CRZ is present (See also Table III for details), which is consistent with a previous study[9], indicating that the position of the PVC corresponds well with that of the CRZ.

Figure 11 also shows that the value of $\bar{r}_{core}/D_c$ typically decreases from Regime I to Regime III, although the extent of the reduction is small for Regime II. For example, at x/L_c = 0.80, the value of $\bar{r}_{core}/D_c$ in Regime II is 20% lower than that in Regime I, while it is approximately 80% lower for Regime III. This is consistent with the PDF of the position of the vortex-core (Fig. 10), showing that a more coherent PVC has a smaller displacement. However, the extent of the reduction in the position of the PVC for each regime is not consistent. For example, the value of $\bar{r}_{core}/D_c$ for Regime III decreases by $\approx$ 50% from 0.058 at x/L_c = 0.27 to 0.03 at x/L_c = 0.80. However, for the case of Regime II, the extent of the reduction in $\bar{r}_{core}/D_c$ is relatively small ($\approx$ 10%) from x/L_c = 0.46 to 0.80 where a PVC is identified. This suggests that the presence of jet precession in the upstream ERZ in Regime II is associated with a substantially lower reduction in the position of the PVC in the downstream CRZ.

Overall, it can be concluded that, for the cases in which the size of the ERZ is larger than, or similar to, that of the CRZ (Regime I and II), the displacement of the PVC remains high throughout

the CRZ region, while for the cases with higher swirl angles and a dominant CRZ (Regime III), the displacement of the PVC is smaller and the movement is more regular.
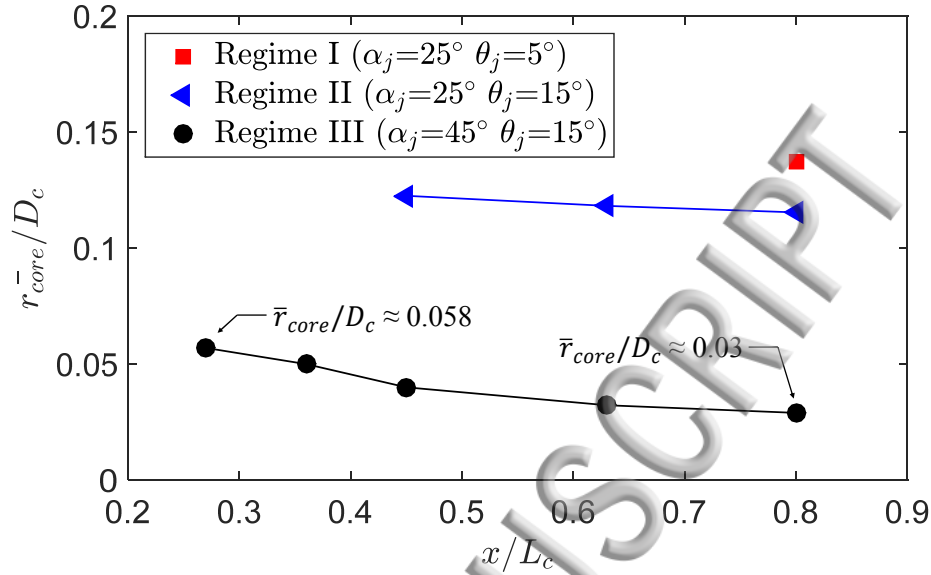
FIG. 11. Averaged vortex-core displacement, normalized by the diameter of the chamber ($\bar{r}_{core}/D_c$) along the axis of the MIJCC for the configurations of Regime I, Regime II and Regime III.

D. Identification of the three-Dimensional flow regimes

Figure 12 presents a schematic diagram of the three rotational flow patterns that have been identified for Regime I ($\alpha_j = 25°$ and $\theta_j = 5°$), Regime II ($\alpha_j = 25°$ and $\theta_j = 15°$) and Regime III ($\alpha_j = 45°$ and $\theta_j = 15°$), using both the measured streamlines and quantitative information from Section III A to III C. A brief summary of the key flow features generated by the MIJCC configurations is listed in Table V and presented below:

(a) Pattern A: Rotation + source

Pattern A is characterized by a rotational flow superimposed on a point source at the cylinder axis. The source is associated with the central resulting jet generated by the interaction of multiple inlet-jets. Hence this flow pattern typically occurs in the ERZ where the magnitude of the axial velocity is significantly greater than that of the tangential velocity ($U_x > U_\theta$).

(b) Pattern B: Rotation + sink

Pattern B is characterized by a rotational flow superimposed on a sink at the axis of the chamber. The sink is generated by the combination of a central reverse flow along the axis and a downstream peripheral flow near to the wall region. This flow pattern is present within a CRZ where the magnitude of the tangential velocity is similar to that of the radial velocity ($U_\theta \approx U_r$).

(c) Pattern C: Pure rotation

Pattern C is characterized by a purely rotational flow dominating the radial planes, which is generated by the high magnitude of tangential component from the swirl angle of the multiple inlet-jets. This flow pattern occurs within the CRZ where the tangential velocity is significantly higher than the radial velocity ($U_\theta > U_r$).

19

(a) (b) (c)
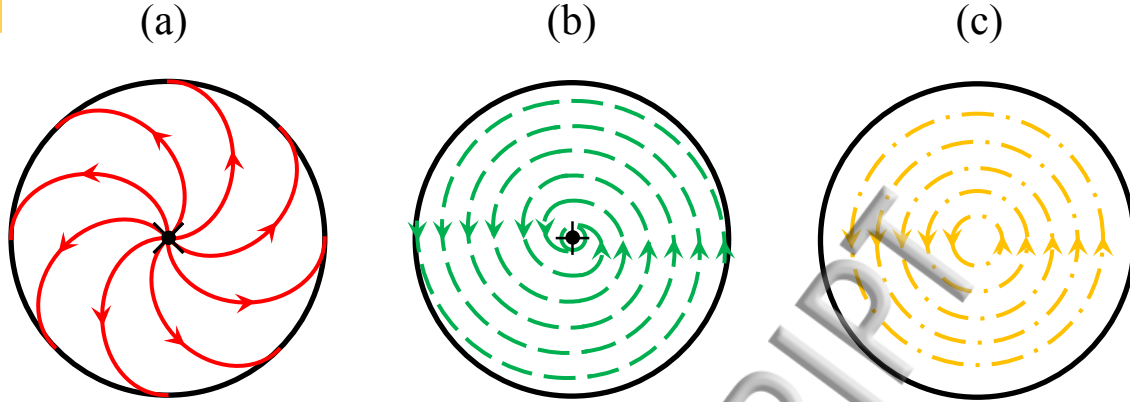
FIG. 12. Schematic diagram of the three rotational flow patterns that have been identified within the MIJCC configurations: (a) Pattern A: rotation + source, (b) Pattern B: rotation + sink, (c) Pattern C: pure rotation. Here the "×" denotes the source and "+" is the sink.

TABLE V. Definition of rotational flow patterns within the MIJCC configurations equipped rotationally-symmetric multiple-jets.

Rotational flow	Flow direction	Recirculation zone	Source	Sink	Swirl strength
Pattern A (rotation+source)	Outwardly spiraling	ERZ	Yes	No	Weak ($U_\theta \approx 0.02 U_e$)
Pattern B (rotation+sink)	Inwardly spiraling	CRZ	No	Yes	Medium ($U_\theta \approx 0.04 U_e$)
Pattern C (pure rotation)	Purely tangential	CRZ	No	No	Strong ($U_\theta \approx 0.12 U_e$)

Figure 13 presents the three distinctive rotational flow patterns within the chamber of the MIJCC for the geometric configurations of Regime I, II and III that have been identified using both the flow visualization and quantitative data. The axial extent of the ERZ and CRZ regions within the MIJCC chamber are also identified by the use of highlighting with red and purple colors, respectively. The results show that the presence of Pattern A corresponds well with the ERZ, while Patterns B and C are typically associated with a CRZ, as expected. However, it should be noted that Pattern B occurs at regions for which the downstream end of the ERZ is located at $x/L_c \geq 0.36$, labelled with a red dashed-line (i.e., $0.63 \leq x/L_c \leq 0.80$ for Regime I, and $0.36 \leq x/L_c \leq 0.45$ for Regime II), while Pattern B is totally absent for Regime III where the ERZ is expected to be located at further upstream ($x/L_c < 0.27$). This finding indicates that the position and size of the ERZ has a controlling influence on the presence of Pattern B (rotational flow with a sink), which in turn suggests that Pattern B tends to be only generated within the transition region between the ERZ and CRZ. This is also consistent with the transition from a forced to Rankine vortexes as discussed in Fig.6. Taken together, it can be concluded that a change from Regimes I to III eliminates Pattern A and leads to the dominance of Pattern C, consistent with the change in the relative significance of the ERZ and CRZ from Regime I to III.
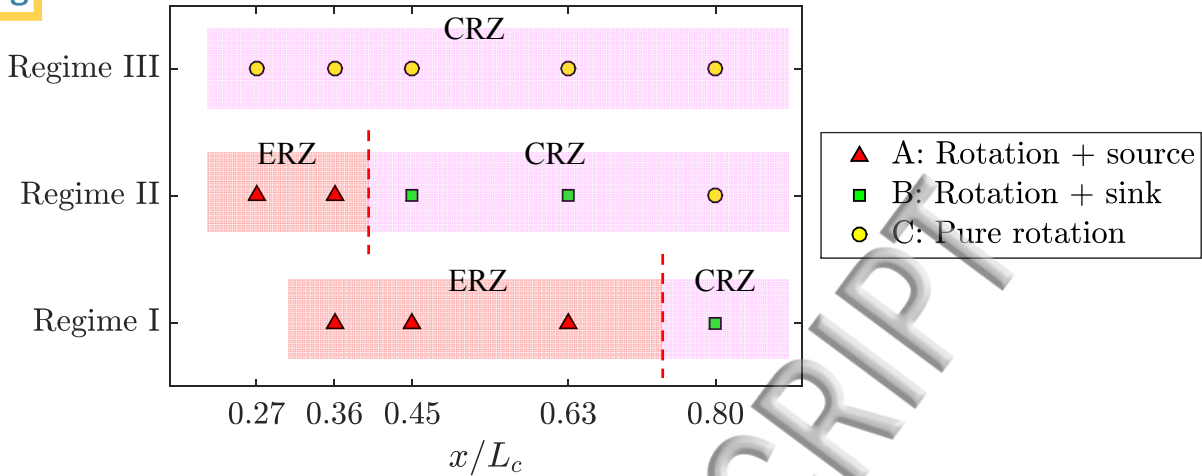
FIG. 13. Map of the key rotational flow patterns as a function of the Regimes I, II and III within the rotationally-symmetric MIJCC configurations. The ERZ and CRZ are highlighted with red and purple colors, respectively.

Figure 14 presents a schematic diagram of the three flow regimes that have been identified within the MIJCC configurations. The data for the x-r plane (axial) have been adapted from our previously published work[7], while that for the r-θ plane (tangential) were obtained from the Pattern A, B and C reported in Fig. 12. The detailed description of the key flow features for the x-r plane is discussed by Long *et al.*[7].

(a) Regime I: Dominant ERZ + weak CRZ + low swirl flow.

Regime I is characterized by the presence of a dominant ERZ and a small downstream CRZ within the cylindrical chamber of the MIJCC. The rotational flows with a source (Pattern A) and a sink (Pattern B) are associated with the main ERZ and the weak CRZ regions, respectively. The swirl strength in this regime is weak, with the majority of the flow being in the axial direction of the chamber. The displacement of the PVC in this regime is the greatest of all cases investigated here.

(b) Regime II: ERZ + CRZ + medium swirl flow.

Regime II is characterized by a strong ERZ and CRZ within the cylindrical chamber, with the axial extent of the ERZ and CRZ is relatively similar. The extent of the Pattern A and B is greater than that for Regime I, while a purely rotational flow (Pattern C) occurs at the downstream region of the chamber. Hence, the swirl strength for this regime is significantly greater than that for Regime I, although the displacement of the core of the PVC is smaller than that for Regime I.

(c) Regime III: Weak ERZ + dominant CRZ + high swirl flow.

Regime III is characterized by the dominance of a CRZ within the chamber, while the ERZ is limited to the conical section of the chamber. Patterns C is recorded for all radial planes downstream from the jet merging point. This regime is also characterized by a significant swirling flow (the most significant among the three identified regimes). Importantly, the PVC in this regime is mostly regular and stable.
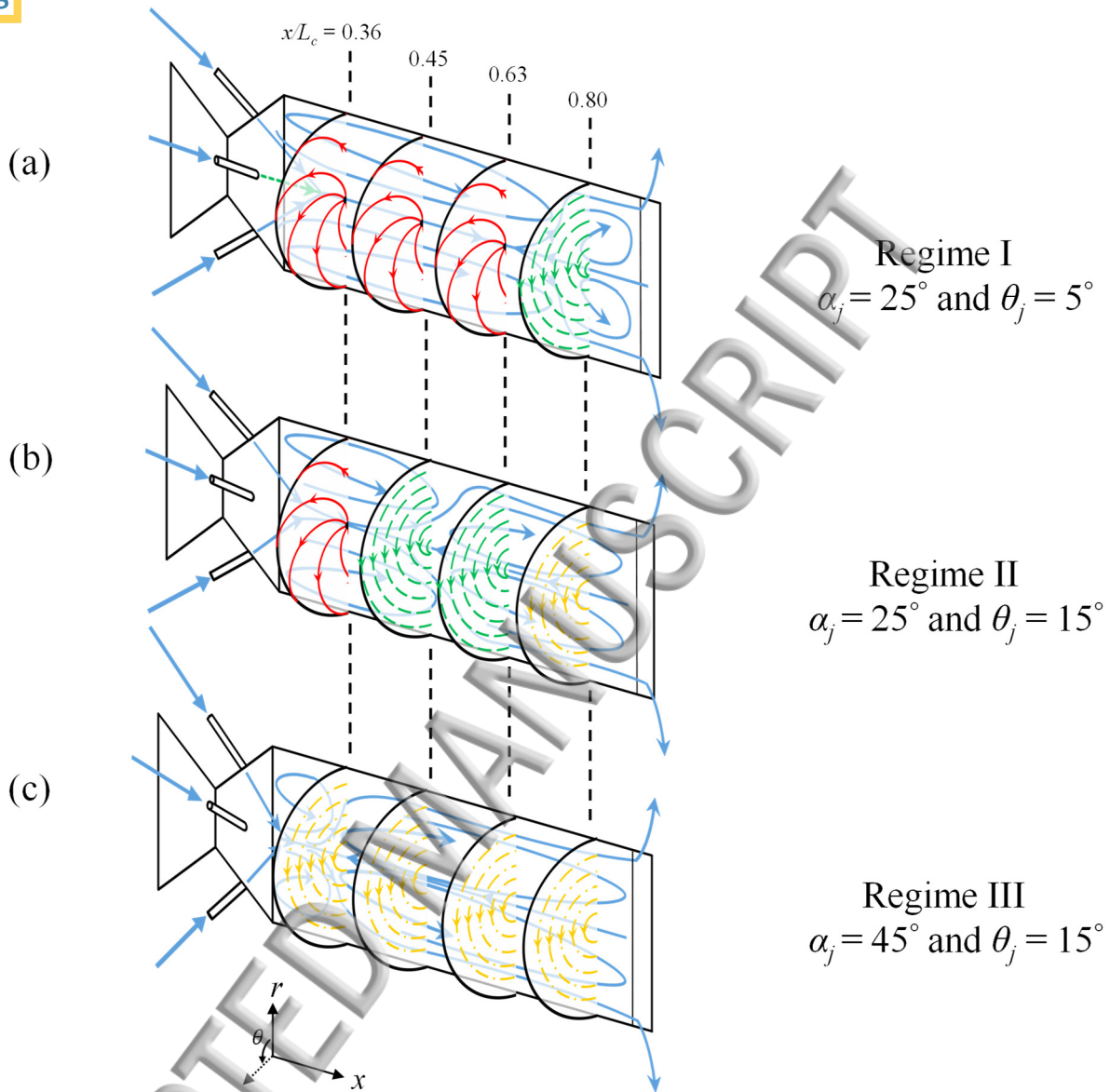
FIG. 14. Schematic diagrams showing the major flow features for the axial plane (across the axis) and four radial planes (orthogonal to the axis) within the rotationally-symmetric MIJCC configurations.

IV. CONCLUSIONS

In conclusion, new qualitative and quantitative information have been provided to the swirling and precessing flows generated by the Multiple Impinging Jets in a Cylindrical Chamber (MIJCC) with the inclination ($\alpha_j = 25°$ and $45°$) and azimuthal angles ($\theta_j = 5°$ and $15°$):

1. The new findings of the three distinctive flow regimes (Regimes I, II and III) are as follows:

a) The magnitude of tangential velocity U_θ is the strongest [$(U_\theta/U_e)_{max} \approx 0.12$] and is almost independent from the axial locations throughout the chamber for Regime III ($\alpha_j = 45°$ and $\theta_j = 15°$) where a dominant central recirculation zone (CRZ) occurs, while the value of U_θ is relatively weak [$(U_\theta/U_e)_{max} \approx 0.04$] and decays much faster along the axis for the cases where a dominant external recirculation zone (ERZ) is present (e.g., Regime I, $\alpha_j = 25°$ and $\theta_j = 5°$). This indicates that the swirl strength is much stronger and remains higher value for the CRZ than that for the ERZ.

b) The transition from Regime I to Regime III is associated with an increase by 60% to 90% in the magnitude of tangential velocity for a given cross-section (x/L_c) within the chamber, resulting in the absence of a free vortex and the presence of a Rankine (forced and free combined) vortex. This corresponds well with the increase in the size of the CRZ, which is caused by the combined effects of large α_j and θ_j increasing the tangential velocity.

c) The RMS (root-mean-square) of tangential velocity (u'_θ) was found to be small and relatively flat for the CRZ, but typically higher for the ERZ. This is associated with the unsteady merging point of the multiple inlet-jets within the ERZ. It was also found that a pronounced peak of the RMS velocities for axial, radial and tangential directions (u'_x, u'_r and u'_θ) occurs within the central region for Regime III. This indicates that a dominant CRZ in Regime III amplifies significantly the level of turbulent fluctuations within the central region of a cylindrical chamber.

d) Three rotational flow patterns were identified within Regimes I, II and III, depending on the relative significance of the ERZ and CRZ:
   - Pattern A: rotational flow superimposed on a source (for the ERZ with a weak swirl $U_x > U_\theta$);
   - Pattern B: rotational flow superimposed on a sink (for the CRZ with a medium swirl $U_\theta \approx U_r$);
   - Pattern C: pure rotation (for the CRZ with a high-swirled flow $U_\theta > U_r$).

2. A precessing vortex core (PVC) was found to occur for all cases investigated here. The key findings of the PVC are as follows:

   a) The axial extent of the regions in which a PVC can be identified is the greatest for Regime III and the least for Regime I. This corresponds well with the axial extent of the CRZ for Regimes I, II and III, indicating that the position of the PVC depends strongly on the size of the CRZ.

   b) The significance of the PVC tends to be amplified for small swirl angles (e.g., $\theta_j = 5°$), but to be inhibited for higher swirl angles (e.g., $\theta_j = 15°$). This is evidenced by up to 80% smaller displacement of the vortex-core (r_{core}) relative to the centre of the chamber for Regime III than that for Regime I.

   c) The value of r_{core} was found to be reduced along the axis of the chamber for all three flow regimes. However, the value of r_{core} is reduced by up to 50% for Regime III, but

23

only 10% for Regimes II. This indicates that a strong interaction of inlet-jets within the upstream ERZ for Regime II tends to retain the displacement of the PVC within the CRZ.
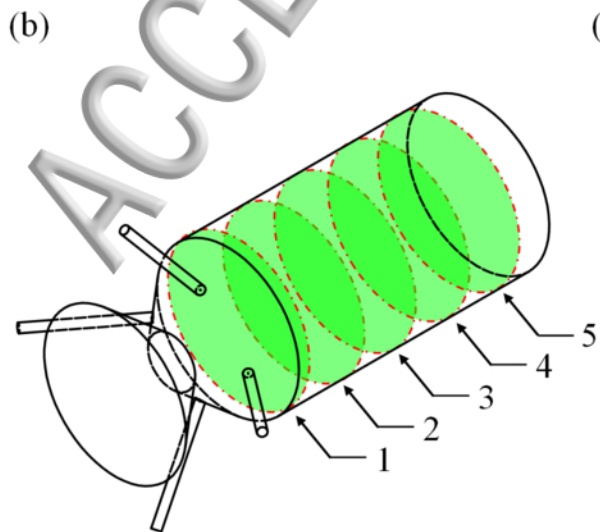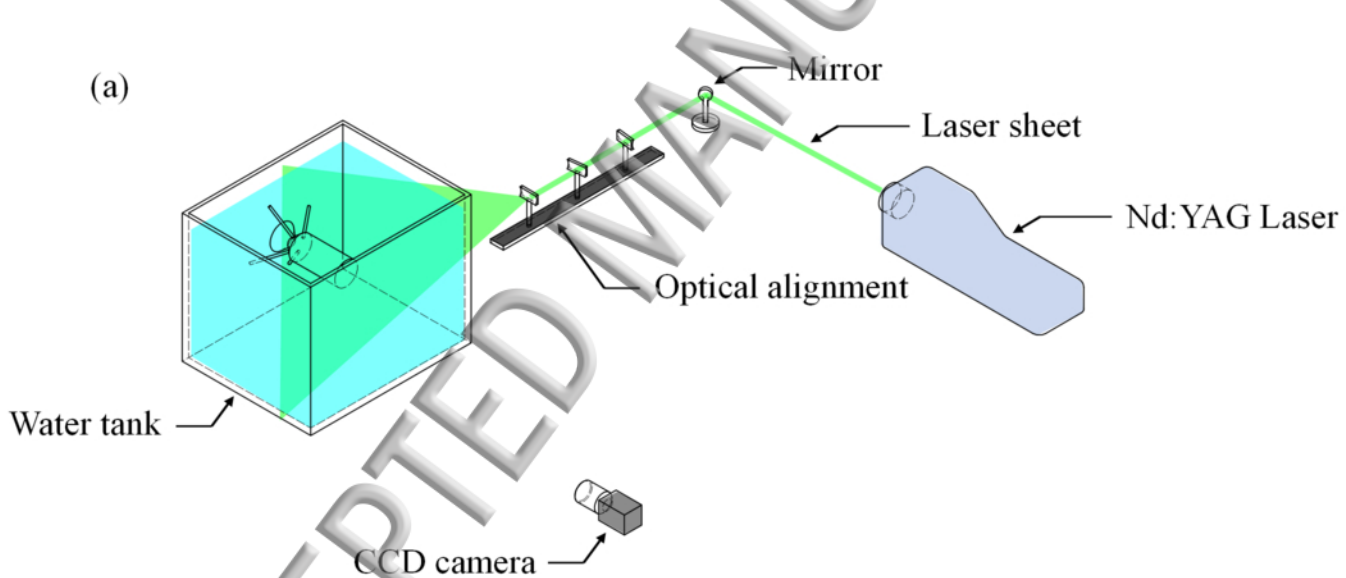
ACKNOWLEDGEMENT

[1] G. Cox, "Multiple jet correlations for gas turbine engine combustor design," J. Eng. Power **98**, 265 (1976).

[2] E. Koepf, W. Villasmil, and A. Meier, "High Temperature Flow Visualization and Aerodynamic Window Protection of a 100-kW th Solar Thermochemical Receiver-reactor for ZnO Dissociation," Energy Procedia **69**, 1780 (2015).

[3] T. Boushaki, and J.-C. Sautet, "Characteristics of flow from an oxy-fuel burner with separated jets: influence of jet injection angle," Exp. Fluids **48**, 1095 (2010).

[4] T. Chammem, H. Mhiri, and O. Vauquelin, "Experimental and computational investigation of Reynolds number effect on the longitudinal ventilation in large enclosure of twin inclined jets," Build. Environ. **67**, 87 (2013).

[5] H. J. Hussein, S. P. Capp, and W. K. George, "Velocity measurements in a high-Reynolds-number, momentum-conserving, axisymmetric, turbulent jet," J. Fluid Mech. **258**, 31 (1994).

[6] S. Long, T. C. W. Lau, A. Chinnici, Z. F. Tian, B. B. Dally, and G. J. Nathan, "Experimental and numerical investigation of the iso-thermal flow characteristics within a cylindrical chamber with multiple planar-symmetric impinging jets," Phys. Fluids **29**, 105111 (2017).

[7] S. Long, T. C. W. Lau, A. Chinnici, Z. F. Tian, B. B. Dally, and G. J. Nathan, "Iso-thermal flow characteristics of rotationally symmetric jets generating a swirl within a cylindrical chamber," Phys. Fluids **30**, 055110 (2018).

[8] S. Long, T. C. W. Lau, A. Chinnici, Z. F. Tian, B. B. Dally, and G. J. Nathan, "The influence of aspect ratio on the iso-thermal flow characteristics of multiple confined jets," Phys. Fluids **30**, 125108 (2018).

[9] N. Syred, "A review of oscillation mechanisms and the role of the precessing vortex core (PVC) in swirl combustion systems," Prog. Energy Combust. Sci. **32**, 93 (2006).

[10] G. Nathan, D. Battye, and P. Ashman, "Economic evaluation of a novel fuel-saver hybrid combining a solar receiver with a combustor for a solar power tower," Appl. Energy **113**, 1235 (2014).

[11] A. Chinnici, Z. F. Tian, J. H. Lim, G. J. Nathan, and B. B. Dally, "Comparison of system performance in a hybrid solar receiver combustor operating with MILD and conventional combustion. Part I: Solar-only and combustion-only employing conventional combustion," Sol. Energy **147**, 489 (2017).

[12] A. Chinnici, Z. F. Tian, J. H. Lim, G. J. Nathan, and B. B. Dally, "Comparison of system performance in a hybrid solar receiver combustor operating with MILD and conventional combustion. Part II: Effect of the combustion mode," Sol. Energy **147**, 479 (2017).

[13] M. Escudier, A. Nickson, and R. Poole, "Influence of outlet geometry on strongly swirling turbulent flow through a circular tube," Phys. Fluids **18**, 125103 (2006).

24

[14] P. Wang, X.-S. Bai, M. Wessman, and J. Klingmann, "Large eddy simulation and experimental studies of a confined turbulent swirling flow," Phys. Fluids **16**, 3306 (2004).

[15] Y. Wang, X. Wang, and V. Yang, "Evolution and transition mechanisms of internal swirling flows with tangential entry," Phys. Fluids **30**, 013601 (2018).

[16] J. Jiao, Z. Liu, and Y. Zheng, "Evaluations and modifications on Reynolds stress model in cyclone simulations," Chem. Eng. Technol. **30**, 15 (2007).

[17] T. Chammem, O. Vauquelin, and H. Mhiri, "Performance evaluation of alternative tunnel longitudinal ventilation systems using two inclined jets," Tunnel. Underground Space Technol. **41**, 53 (2014).

[18] Y. Wang, and V. Yang, "Central recirculation zones and instability waves in internal swirling flows with an annular entry," Phys. Fluids **30**, 013602 (2018).

[19] A. Ridluan, S. Eiamsa-ard, and P. Promvonge, "Numerical simulation of 3D turbulent isothermal flow in a vortex combustor," ICHMT **34**, 860 (2007).

[20] A. Z'graggen, P. Haueter, D. Trommer, M. Romero, J. De Jesus, and A. Steinfeld, "Hydrogen production by steam-gasification of petroleum coke using concentrated solar power—II Reactor design, testing, and modeling," Int. J. Hydrogen Energy **31**, 797 (2006).

[21] N. Ozalp, M.-H. Chien, and G. Morrison, "Computational fluid dynamics and particle image velocimetry characterization of a solar cyclone reactor," J Sol Energy Eng **135**, 031003 (2013).

[22] L. O. Schunk, P. Haeberling, S. Wepf, D. Wuillemin, A. Meier, and A. Steinfeld, "A receiver-reactor for the solar thermal dissociation of zinc oxide," J Sol Energy Eng **130**, 021009 (2008).

[23] D. Hirsch, and A. Steinfeld, "Solar hydrogen production by thermal decomposition of natural gas using a vortex-flow reactor," Int. J. Hydrogen Energy **29**, 47 (2004).

[24] G. Nathan, S. Hill, and R. Luxton, "An axisymmetric 'fluidic'nozzle to generate jet precession," J. Fluid Mech. **370**, 347 (1998).

[25] G. Schneider, D. Froud, N. Syred, G. Nathan, and R. Luxton, "Velocity measurements in a precessing jet flow using a three dimensional LDA system," Exp. Fluids **23**, 89 (1997).

[26] N. Grosjean, L. Graftieaux, M. Michard, W. Hübner, C. Tropea, and J. Volkert, "Combining LDA and PIV for turbulence measurements in unsteady swirling flows," Meas. Sci. Technol. **8**, 1523 (1997).

[27] F. Martinelli, A. Olivani, and A. Coghe, "Experimental analysis of the precessing vortex core in a free swirling jet," Exp. Fluids **42**, 827 (2007).

[28] N. Syred, and J. Beer, "Combustion in swirling flows: a review," Combust. Flame **23**, 143 (1974).

[29] A. Chinnici, Y. Xue, T. C. Lau, M. Arjomandi, and G. J. Nathan, "Experimental and numerical investigation of the flow characteristics within a Solar Expanding-Vortex Particle Receiver-Reactor," Sol. Energy **141**, 25 (2017).

[30] A. Valera-Medina, N. Syred, and A. Griffiths, "Visualisation of isothermal large coherent structures in a swirl burner," Combust. Flame **156**, 1723 (2009).

[31] M. Bauerheim, F. Nicoud, and T. Poinsot, "Progress in analytical methods to predict and control azimuthal combustion instability modes in annular chambers," Phys. Fluids **28**, 021303 (2016).

[32] S. I. Voropayev, X. Sanchez, C. Nath, S. Webb, and H. J. S. Fernando, "Evolution of a confined turbulent jet in a long cylindrical cavity: Homogeneous fluids," Phys. Fluids **23**, 115106 (2011).

[33] N. Syred, and K. Dahman, "Effect of high levels of confinement upon the aerodynamics of swirl burners," JEner **2**, 8 (1978).

[34] A. K. Gupta, D. G. Lilley, and N. Syred, "Swirl flows," Tunbridge Wells, Kent, England, Abacus Press, 1984, 488 p. (1984).

[35] D. M. Markovich, S. S. Abdurakipov, L. M. Chikishev, V. M. Dulin, and K. Hanjalić, "Comparative analysis of low- and high-swirl confined flames and jets by proper orthogonal and dynamic mode decompositions," Phys. Fluids **26**, 065109 (2014).

[36] J. Nikuradse, "Gesetzmäßigkeiten der turbulenten Strömung in glatten Rohren," Forsch. Geb. Ingenieurwes. **4**, 44 (1933).

[37] M. Vanierschot, and E. Van den Bulck, "Hysteresis in flow patterns in annular swirling jets," Exp. Therm Fluid Sci. 31, 513 (2007).

[38] M. S. Chong, A. E. Perry, and B. J. Cantwell, "A general classification of three‐dimensional flow fields," Phys. Fluids **2**, 765 (1990).

[39] A. E. Perry, and M. S. Chong, "A description of eddying motions and flow patterns using critical-point concepts," Annu. Rev. Fluid Mech. **19**, 125 (1987).

[40] O. Kitoh, "Experimental study of turbulent swirling flow in a straight pipe," J. Fluid Mech. **225**, 445 (1991).

[41] F. Chang, and V. Dhir, "Turbulent flow field in tangentially injected swirl flows in tubes," Int. J. Heat Fluid Flow **15**, 346 (1994).

[42] A. Hoekstra, J. Derksen, and H. Van Den Akker, "An experimental and numerical study of turbulent swirling flow in gas cyclones," Chem. Eng. Sci. **54**, 2055 (1999).

[43] P. Billant, J.-M. Chomaz, and P. Huerre, "Experimental study of vortex breakdown in swirling jets," J. Fluid Mech. **376**, 183 (1998).

[44] F. Gallaire, and J.-M. Chomaz, "Instability mechanisms in swirling flows," Phys. Fluids **15**, 2622 (2003).

[45] M. Vanierschot, and E. Van den Bulck, "Influence of swirl on the initial merging zone of a turbulent annular jet," Phys. Fluids **20**, 105104 (2008).

[46] J. Volkert, C. Tropea, R. Domann, and W. H¨ubner, "Combined application of particle image velocimetry (PIV) and laser Doppler anemometry, (LDA) to swirling flows under compression," in *Proceedings of the 8th International Symposia on Applications of Laser Techniques to Fluid Mechanics* (Springer-Verlag, 1996), Vol. 19, pp. 1–19.
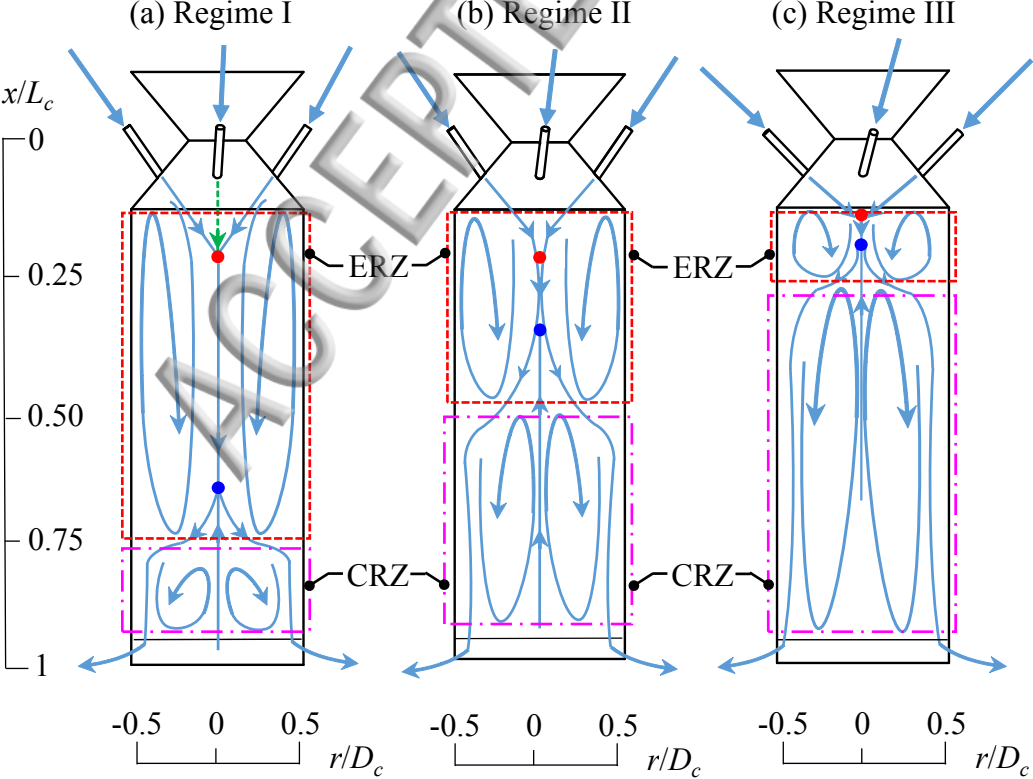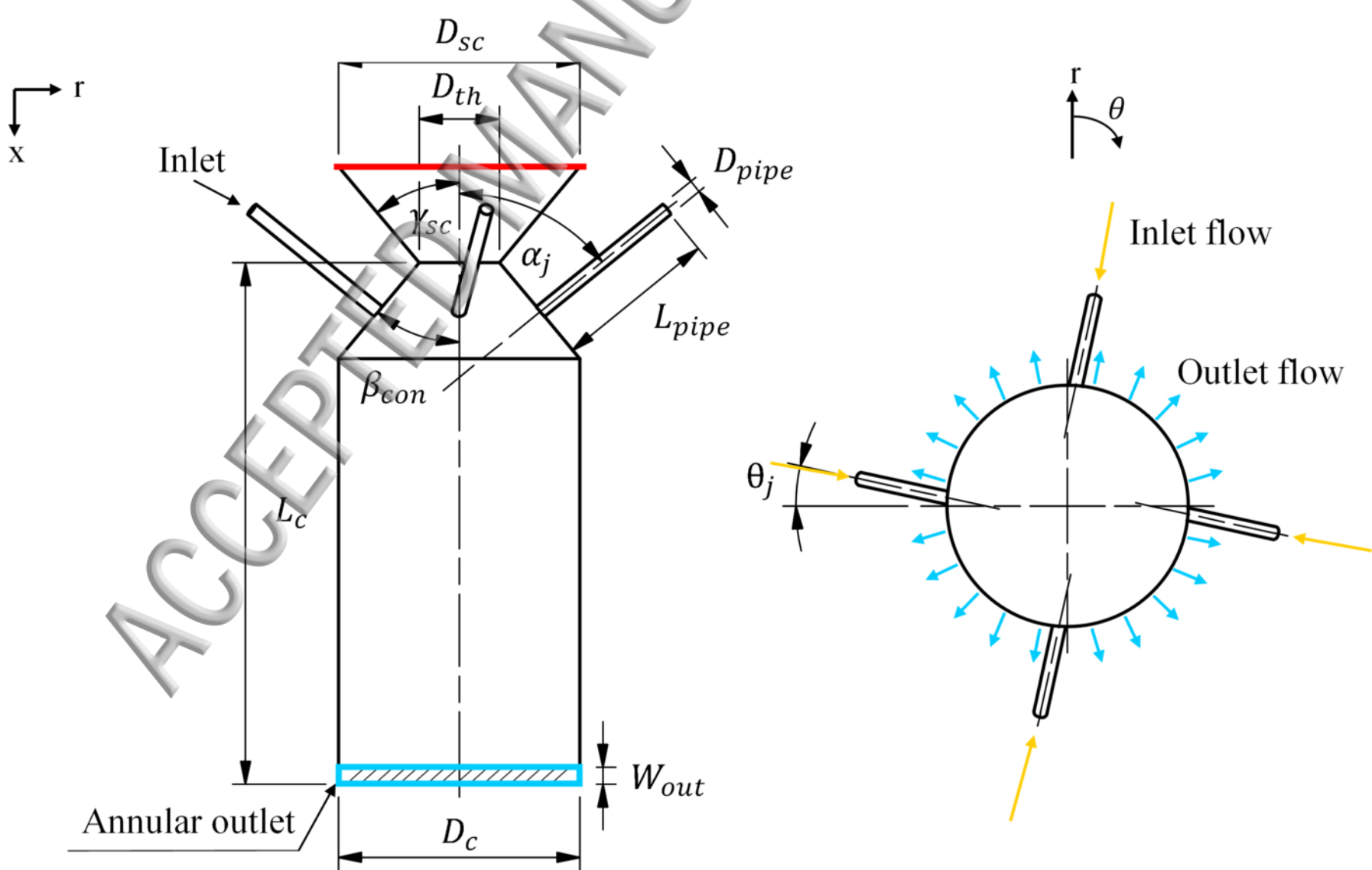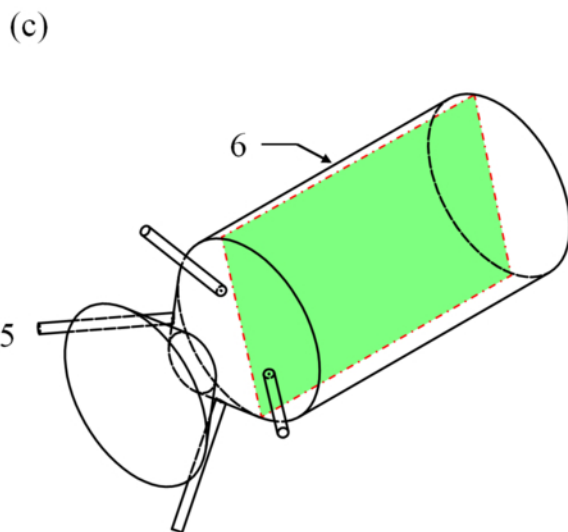
(a) Regime I　　(b) Regime II　　(c) Regime III

(a)

Mirror

Laser sheet

Nd:YAG Laser

Optical alignment

Water tank

CCD camera

(b)

(c)

1
2
3
4
5

6
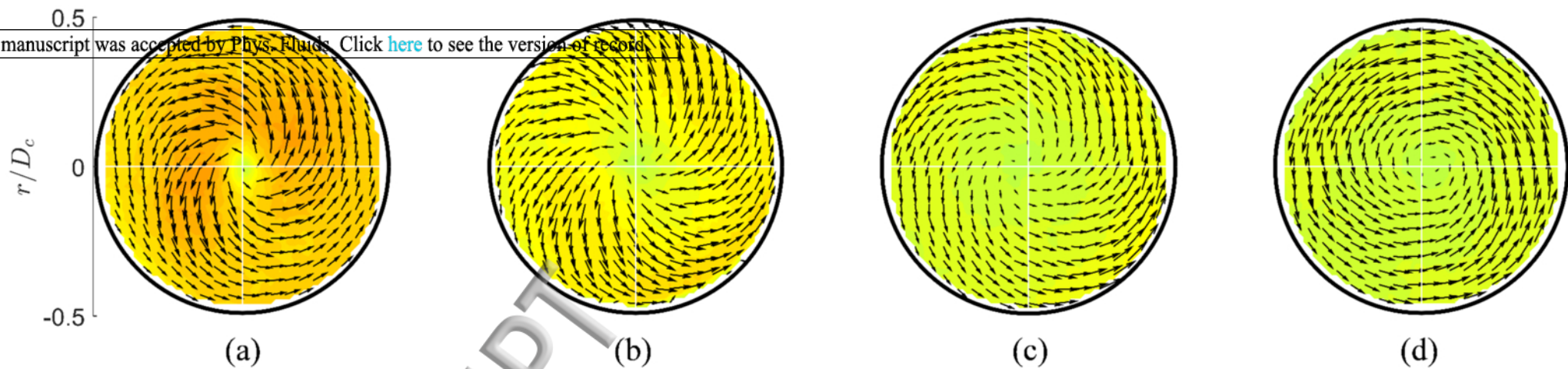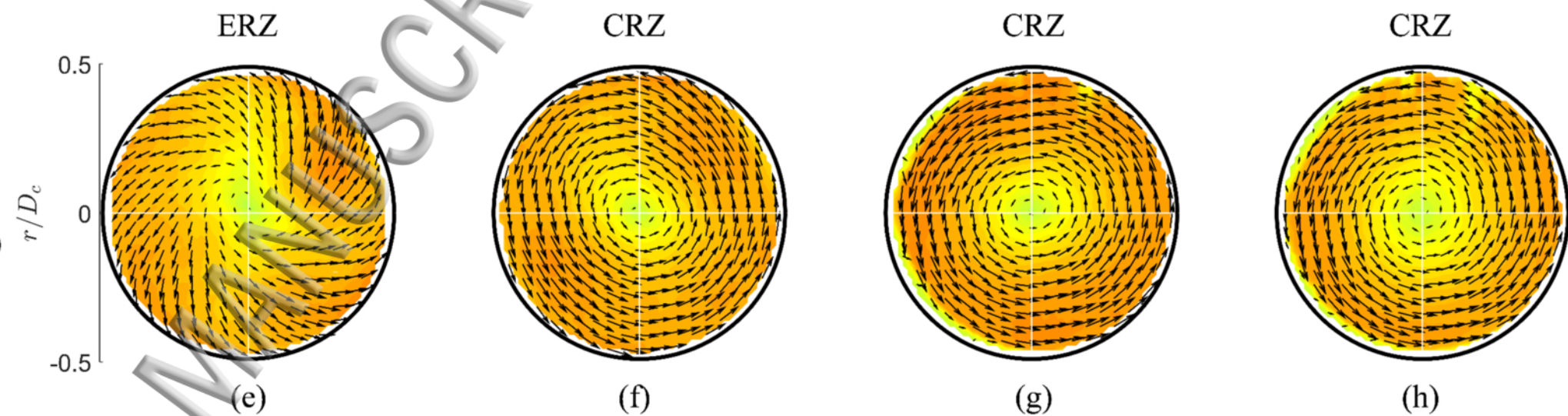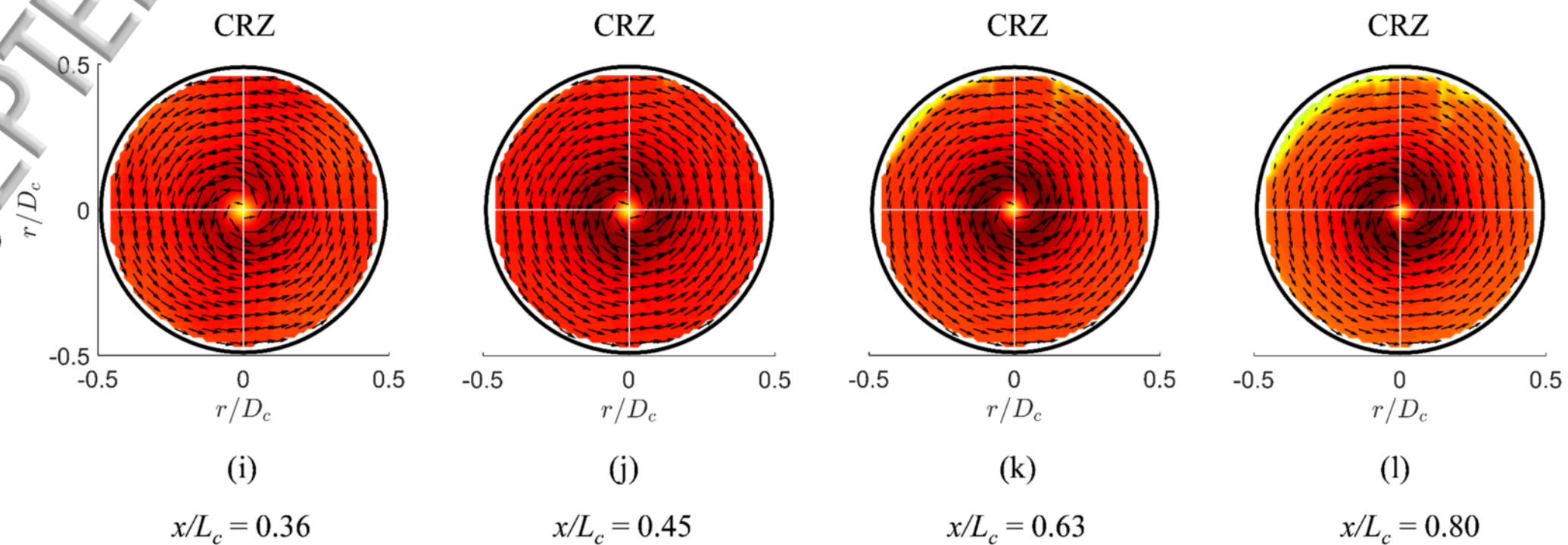
ERZ   ERZ   ERZ   CRZ

Regime I
($\alpha_j = 25°$ and $\theta_j = 5°$)

(a)   (b)   (c)   (d)

ERZ   CRZ   CRZ   CRZ

Regime II
($\alpha_j = 25°$ and $\theta_j = 15°$)
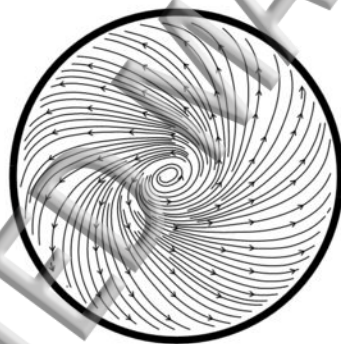
(e)   (f)   (g)   (h)

CRZ   CRZ   CRZ   CRZ

Regime III
($\alpha_j = 45°$ and $\theta_j = 15°$)

(i)   (j)   (k)   (l)

$x/L_c = 0.36$ $x/L_c = 0.45$ $x/L_c = 0.63$ $x/L_c = 0.80$

(a) Regime I ($\alpha_j=25°$ $\theta_j=5°$)

Legend:
- $x/L_c = 0.36$
- $x/L_c = 0.45$
- $x/L_c = 0.63$
- $x/L_c = 0.80$

(b) Regime II ($\alpha_j=25°$ $\theta_j=15°$)

(c) Regime III ($\alpha_j=45°$ $\theta_j=15°$)

Axes: u'_θ/U_e versus r/D_c

(a)

(b)

(a)

(b)

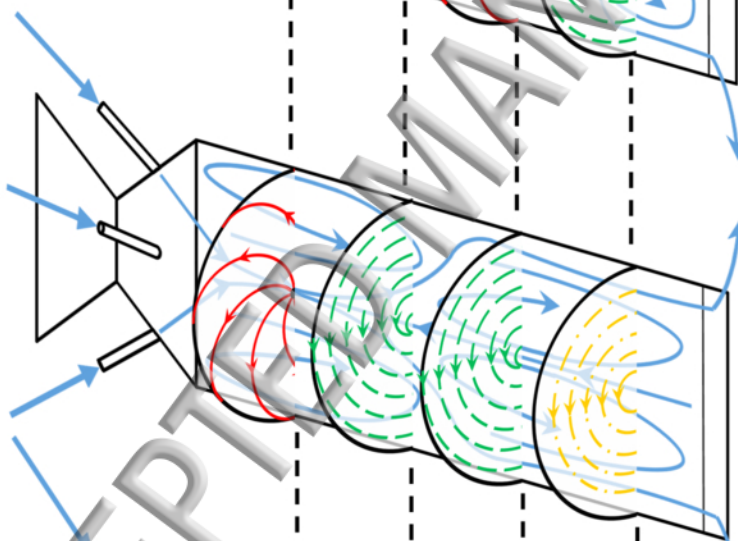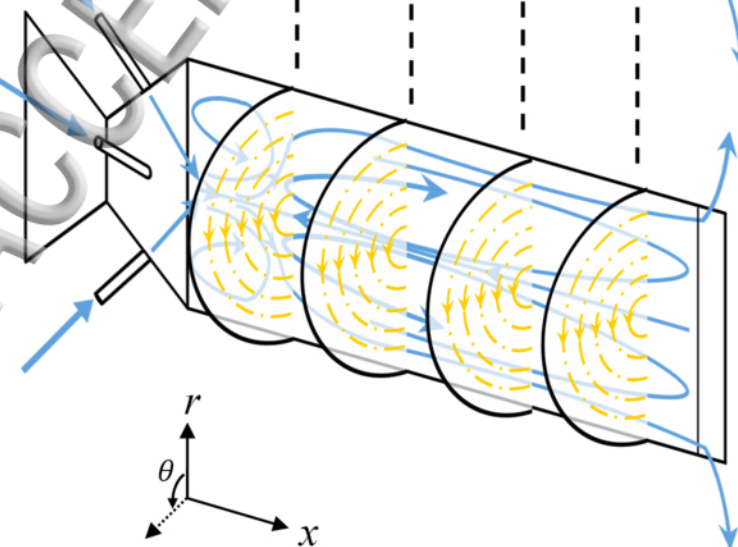(a)   (b)   (c)

(a)

$x/L_c = 0.36$

0.45

0.63

0.80
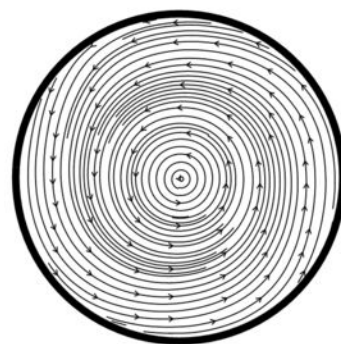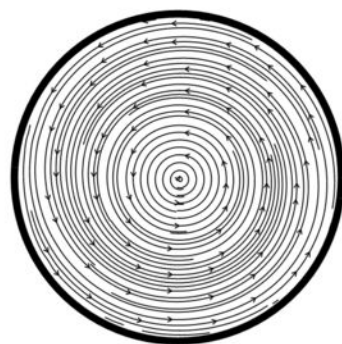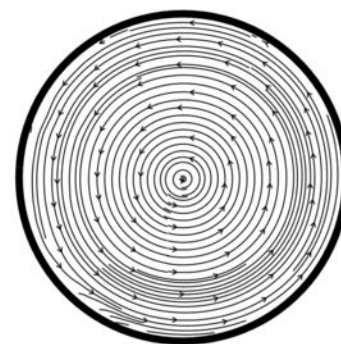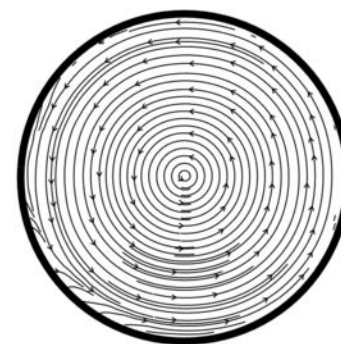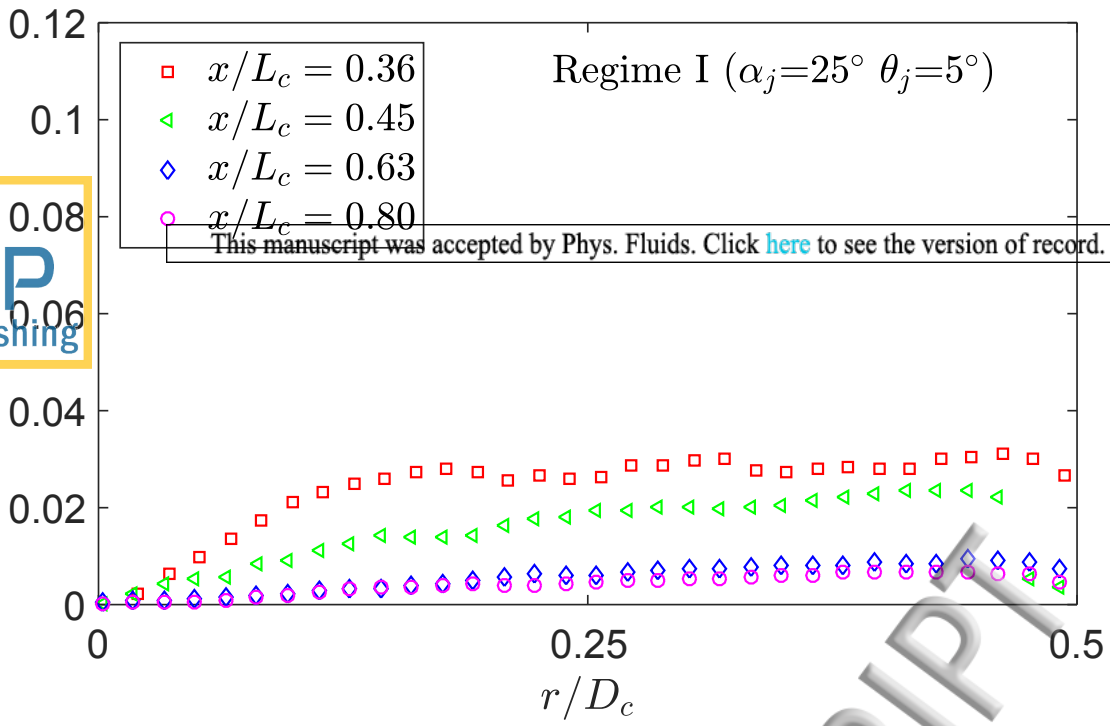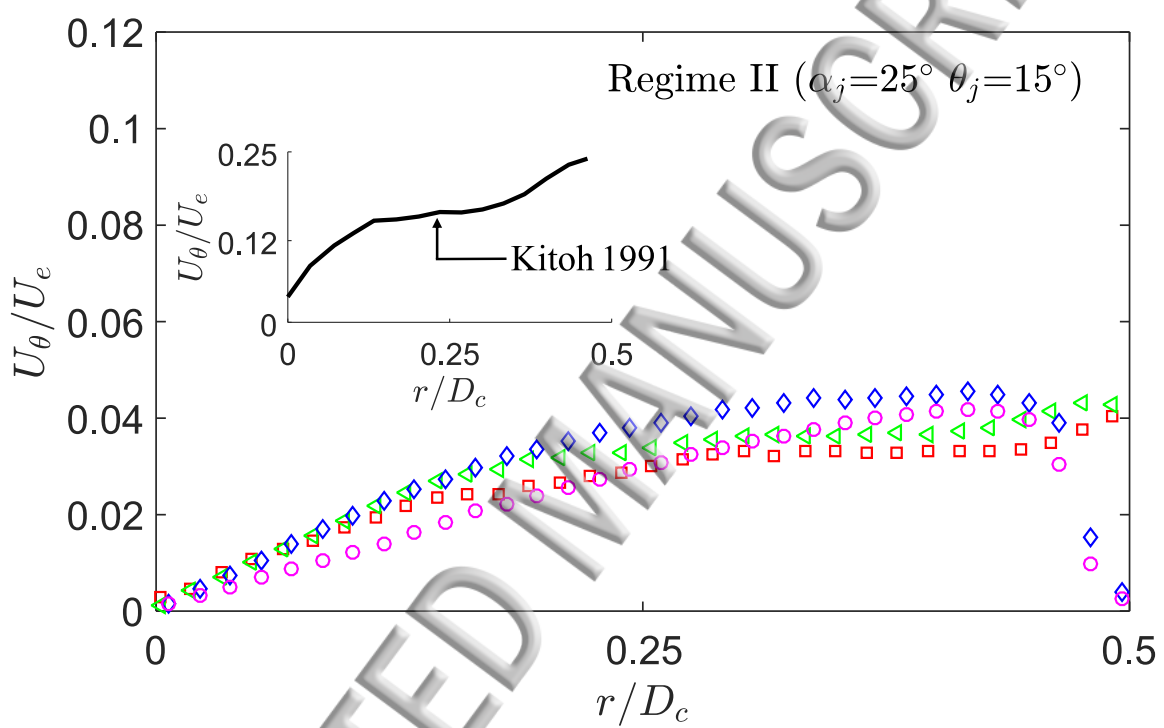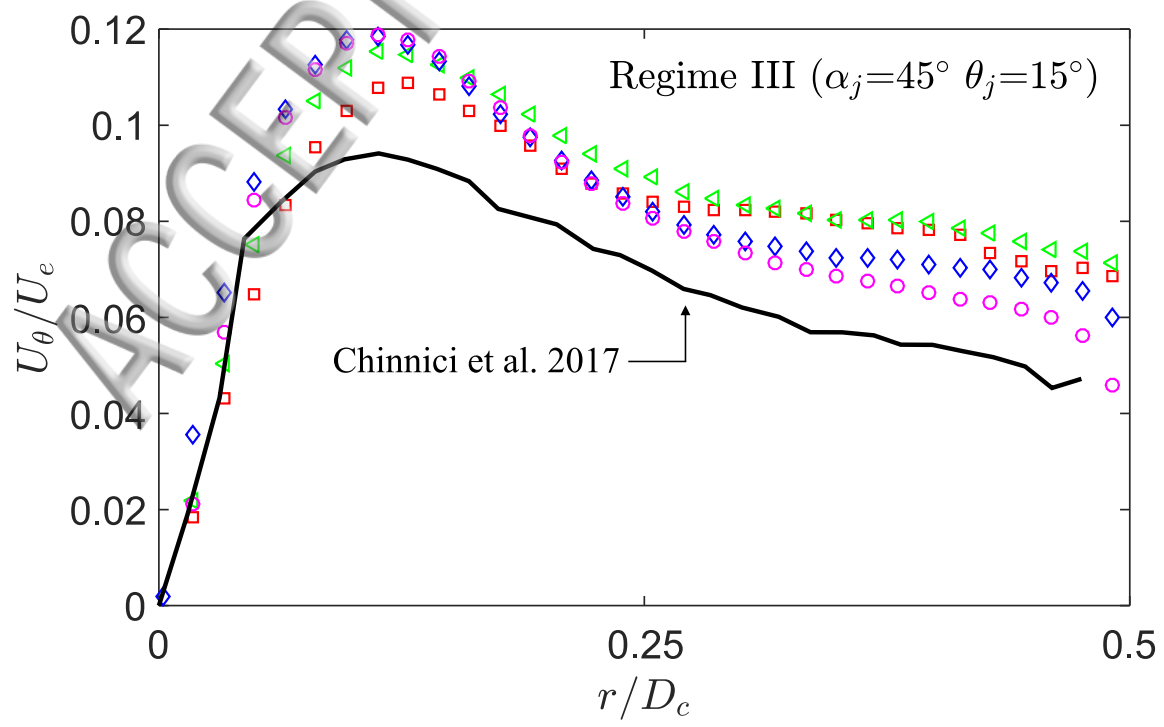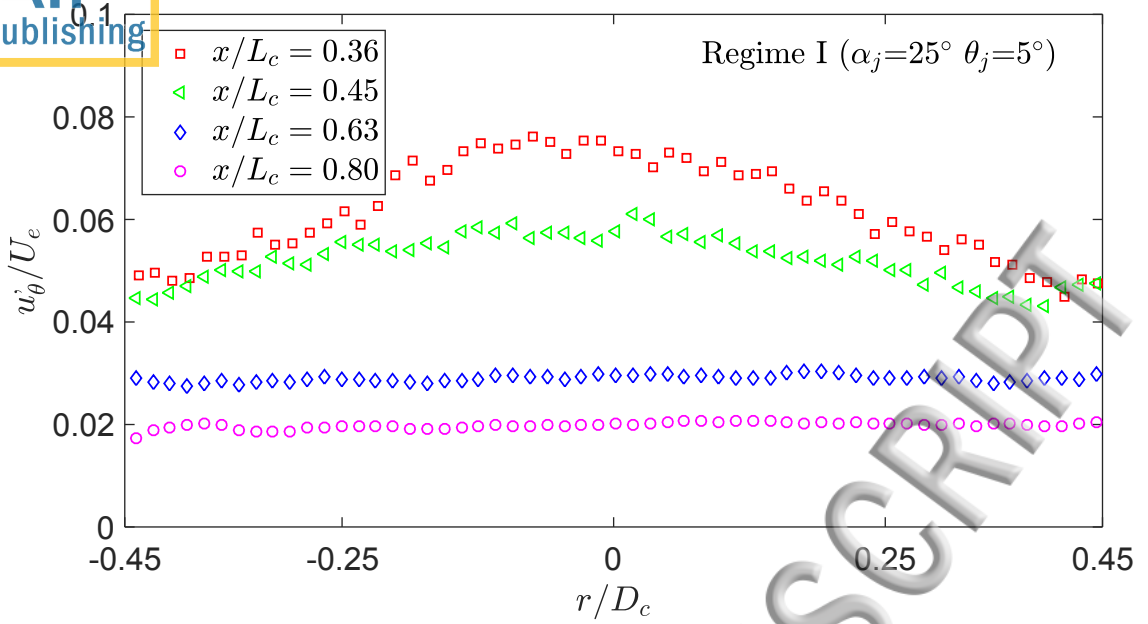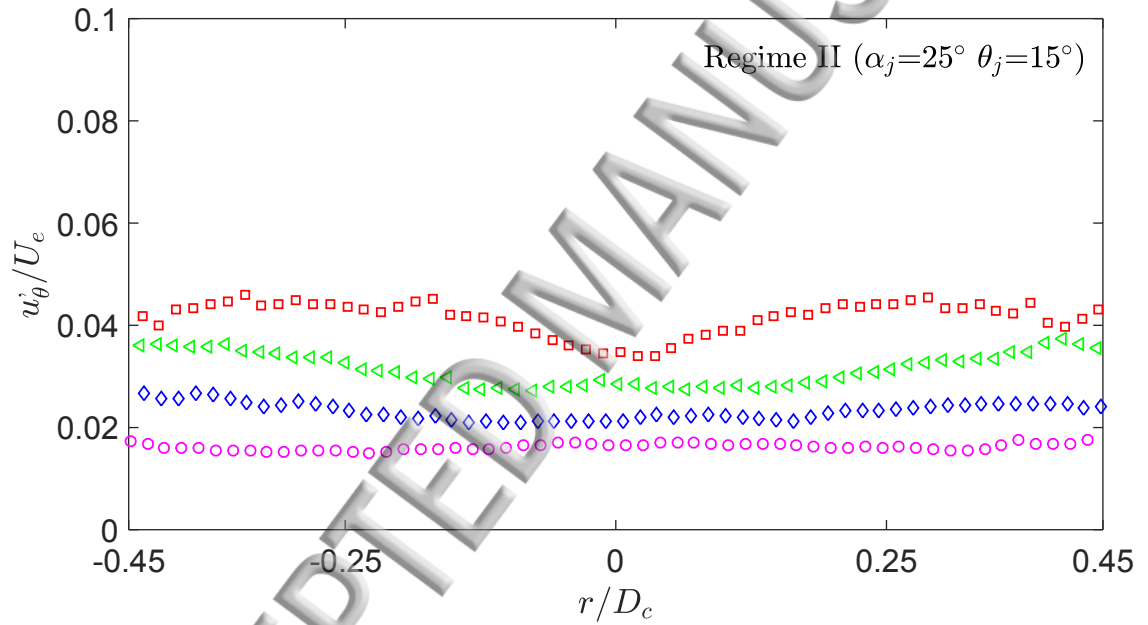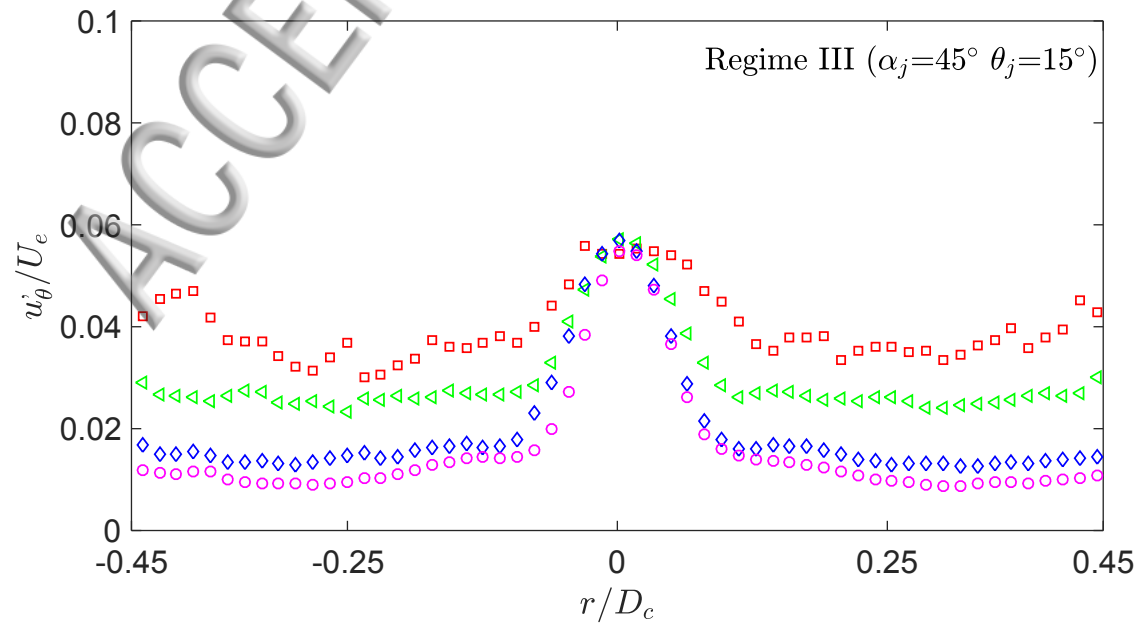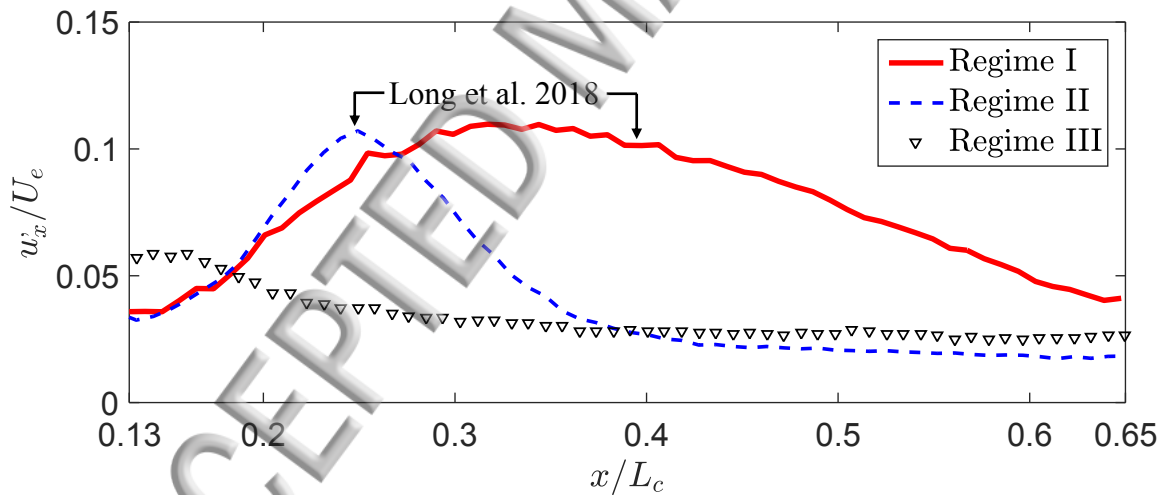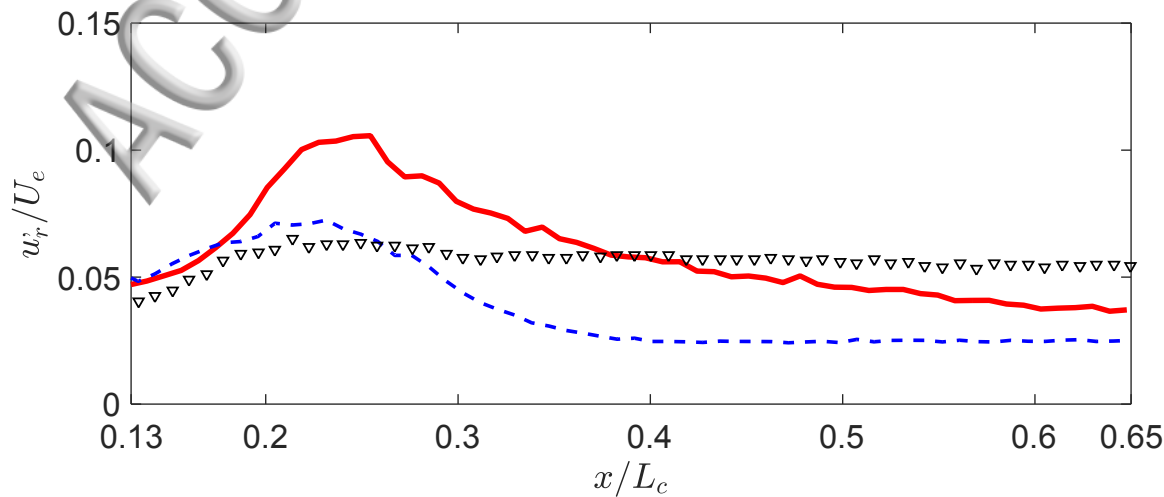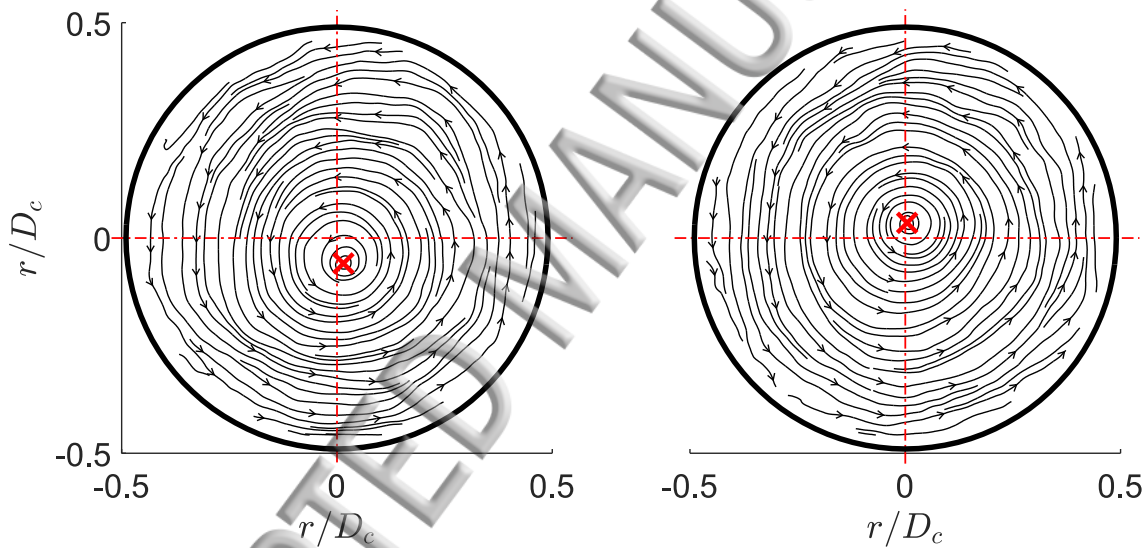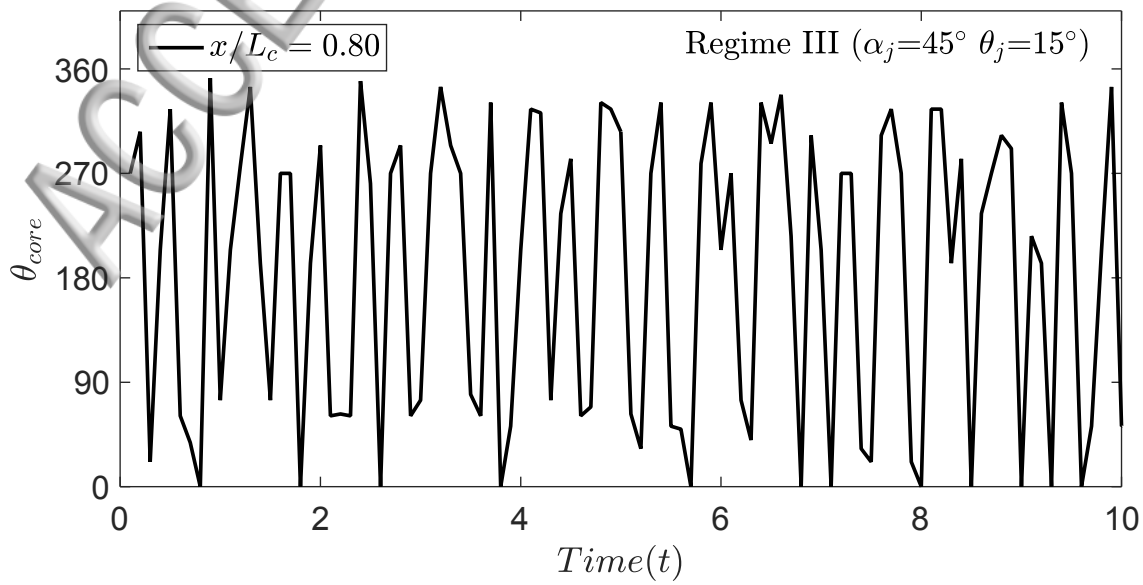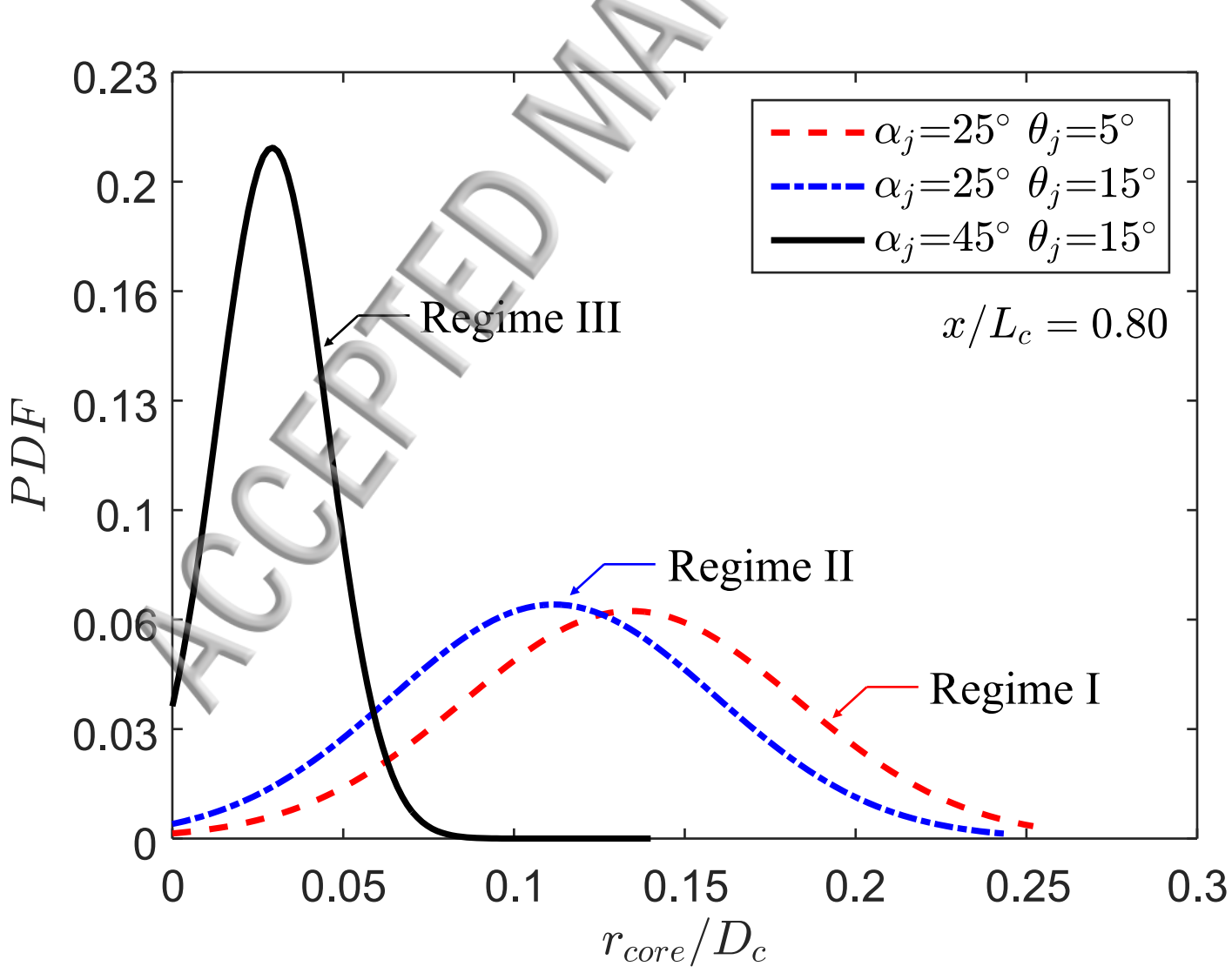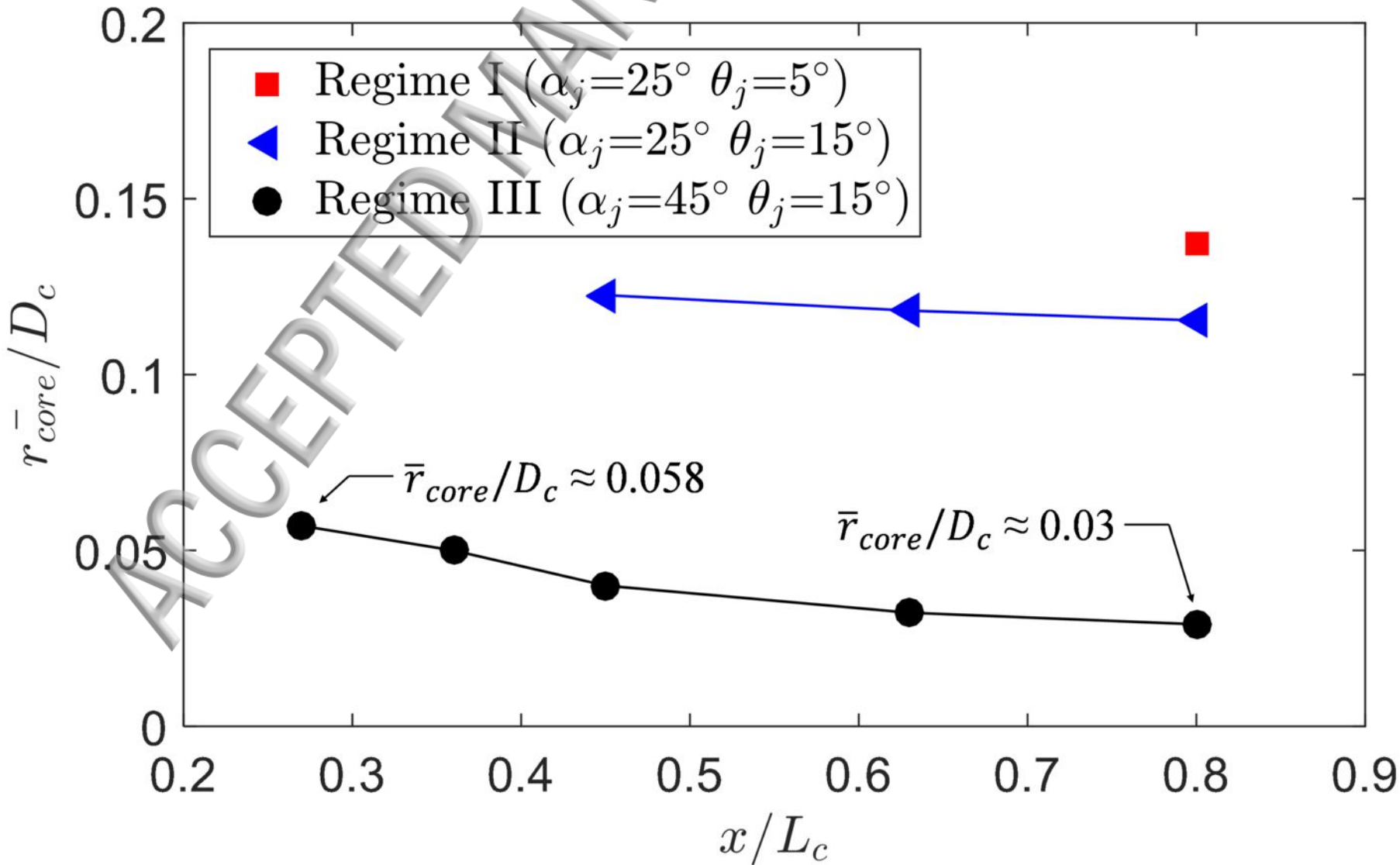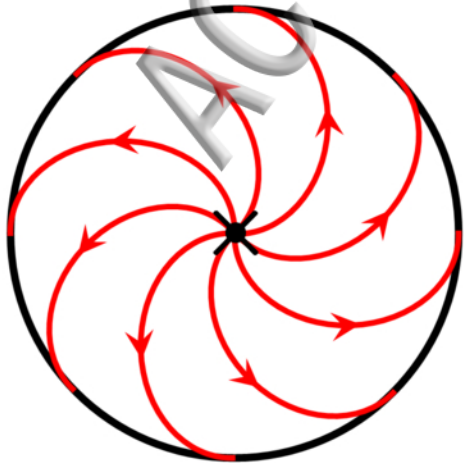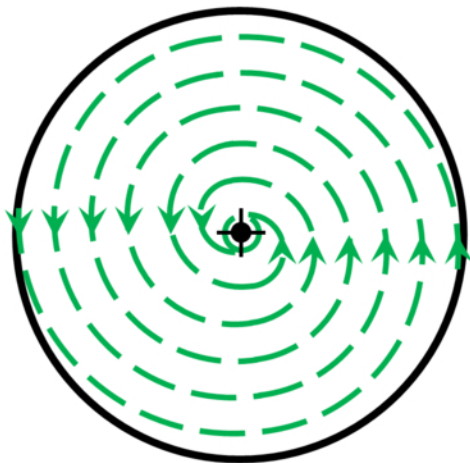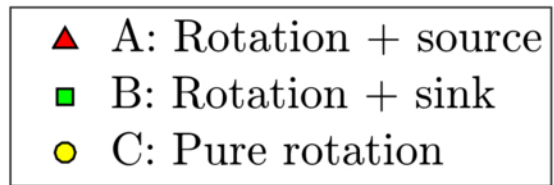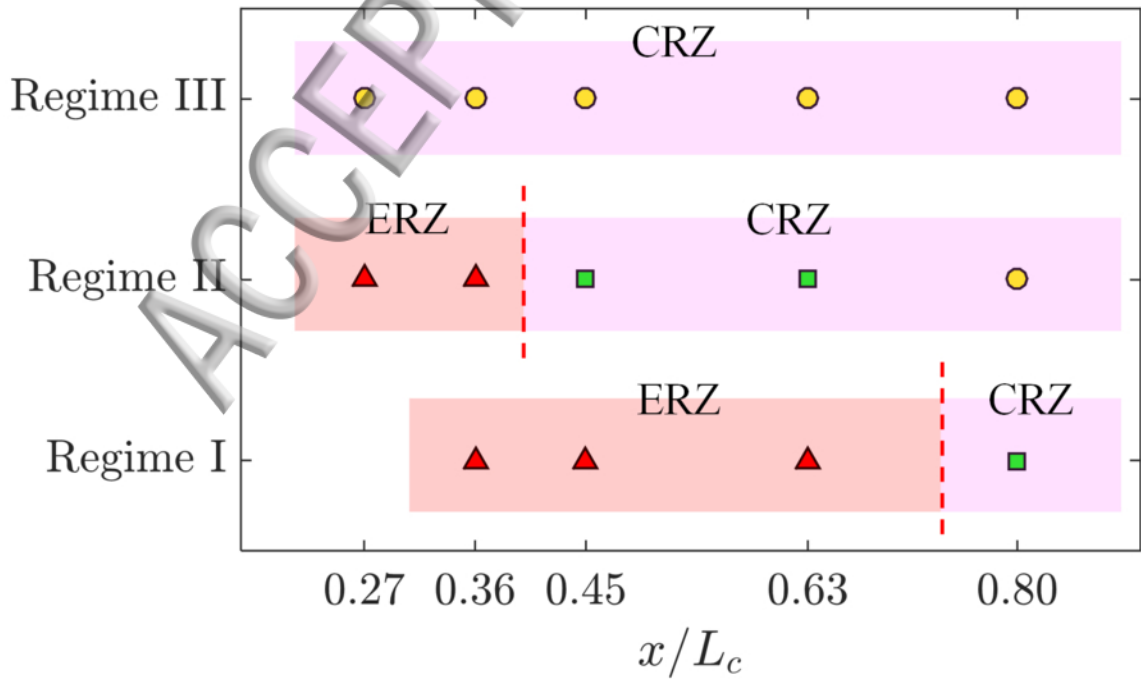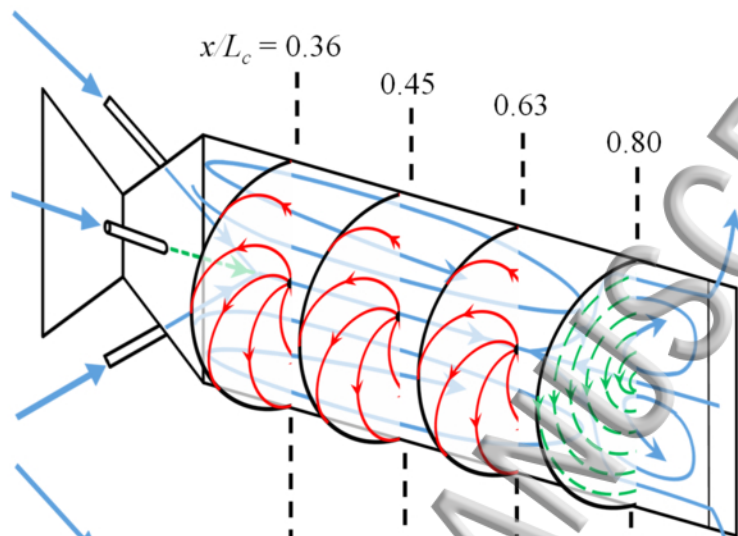
Regime I
$\alpha_j = 25°$ and $\theta_j = 5°$

(b)

Regime II
$\alpha_j = 25°$ and $\theta_j = 15°$

(c)

Regime III
$\alpha_j = 45°$ and $\theta_j = 15°$

r

θ

x